LBL-20519

Lawrence Berkeley Laboratory
UNIVERSITY OF CALIFORNIA

Materials & Molecular
Research Division

MEASUREMENT OF STARK AMPLITUDES IN THE $6^2P_{1/2} \rightarrow 7^2P_{1/2}$ TRANSITION OF ATOMIC THALLIUM

C.E. Tanner
(Ph.D. Thesis)

November 1985

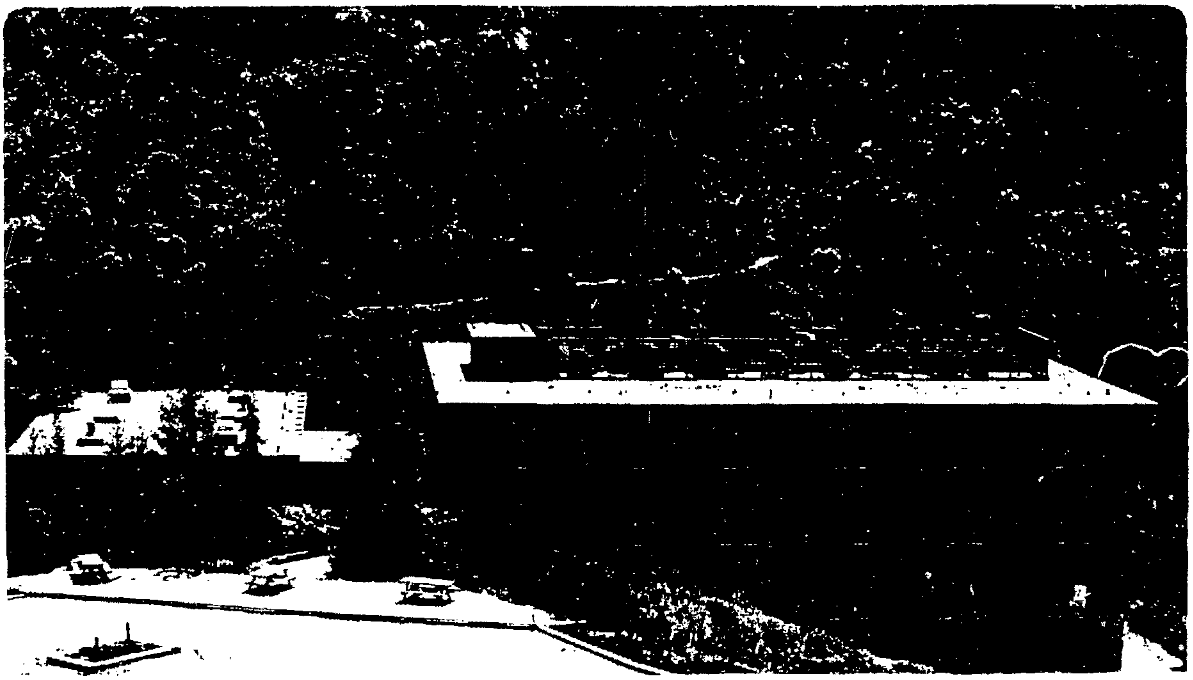

Prepared for the U.S. Department of Energy under Contract DE-AC03-76SF00098

LBL--20519

DE86 005894

MEASUREMENT OF STARK AMPLITUDES IN THE $6^2P_{1/2} \to 7^2P_{1/2}$ TRANSITION OF ATOMIC THALLIUM

Carol Elizabeth Tanner

(Ph.D. Thesis)

Department of Physics and
Lawrence Berkeley Laboratory
University of California
Berkeley, California 94720

This research was supported by the Director, Office of Energy Research, Office of Basic Energy Sciences, Chemical Sciences Division of the U.S. Department of Energy under Contract No. DE-AC03-76SF00098. Laser equipment used in this work is borrowed from the San Francisco Laser Center, supported by the National Science Foundation, NSF Grant No. CHE79-16250 and the National Institute of Health, NIH Grant No. P41 RR01613-02 awarded to the University of California at Berkeley in collaboration with Stanford University.

CONTENTS

MEASUREMENT OF STARK AMPLITUDES IN THE $6^2P_{1/2} \rightarrow 7^2P_{1/2}$ TRANSITION OF ATOMIC THALLIUM

Carol Elizabeth Tanner

(Ph.D. Thesis)

Department of Physics and
Lawrence Berkeley Laboratory
University of California
Berkeley, California 94720

ABSTRACT

This thesis describes the measurement of Stark amplitude coefficients α and β for the $6^2P_{1/2} \rightarrow 7^2P_{1/2}$ transition of ^{205}Tl in an external static electric field $\vec{E}$. The coefficient α is determined by measuring the absorption of linearly polarized 293 nm light ($\hat{\varepsilon} \parallel \vec{E}$) at the $F=1 \rightarrow F'=1$ resonance in a cell with known electric field and interaction length, and calibrated thallium density. Then β is determined from the ratio β^2/α^2 of intensities of the $F=0 \rightarrow F=1$ and $F=0 \rightarrow F=0$ resonance lines in fluorescence. The final results are $\alpha = (1.30 \pm 0.06) \times 10^{-5}\ \mu_0$ cm/V and $\beta = (1.08 \pm 0.05) \times 10^{-5}\ \mu_0$ cm/V (where μ_0 = electron Bohr magneton). β is combined with a previous measurement of Im $\mathcal{E}_p/\beta$ to yield the parity non-conserving electric dipole amplitude $\mathcal{E}_p$.

I. INTRODUCTION

The standard model of electroweak phenomena unifies the electromagnetic and weak interactions in a self consistent, renormalizable theory. This model, introduced by Glashow, Weinberg and Salam, employs the principle of local SU(2)xU(1) gauge invariance (Glashow 61, Salam 68, Weinberg 67). The interaction between fermions is described by exchange of intermediate gauge quanta. The concept of spontaneous symmetry breaking through the Higgs mechanism is used to give mass to the gauge quanta while still allowing renormalizability of the theory (Commins 83). Massive gauge quanta are necessary to insure that the weak force is short range. The standard model predicts four gauge quanta: the massless photon of electrodynamics, and three massive quanta--the charged W^+, W^- and neutral Z° vector bosons--of the weak interaction. The theory was constructed to include the known facts about parity violation in charged weak interactions, but the success of the theory lies in its predictive power. In addition to the familiar interaction between charged weak currents mediated by $W^\pm$, the standard model predicted the existence of previously unobserved neutral current interactions mediated by Z° exchange. In particular, the standard model makes specific predictions about the neutral weak interaction between electrons and nucleons which can have an effect on atomic transitions.

A. Weak Neutral Currents

If the weak interaction is considered in addition to the electromagnetic interaction, an electron and a nucleon may interact by

Z° exchange similar to the exchange of a photon in the electromagnetic interaction. (See Fig. I-1.) Then a transition amplitude can be expressed as the sum of an electromagnetic and a weak amplitude.

$$A = A_{EM} + A_{WEAK} \tag{I.1}$$

The transition probability, proportional to $|A|^2$, will contain an interference term:

$$|A|^2 = |A_{EM} + A_{WEAK}|^2 = |A_{EM}|^2 + A_{WEAK}A_{EM}^* + A_{EM}A_{WEAK}^* + |A_{WEAK}|^2 \ . \tag{I.2}$$

At ordinary laboratory energies, $A_{WEAK} << A_{EM}$, so the weak interaction is not usually considered in atoms. However, since the weak interaction is parity violating, the weak amplitude contains not only a scalar but also a pseudoscalar part:

$$A_{WEAK} = A_{WS} + A_{WP} \ . \tag{I.3}$$

This makes it possible to observe the interference between A_{EM} and A_{WP} because the sign of the latter depends on the handedness of the experimental coordinate system. In an experiment designed to observe the difference in transition rates between a right (R) and a left (L) handed coordinate system, the asymmetry in the transition probability δ can be observed:

$$\delta = \frac{|A_R|^2 - |A_L|^2}{|A_R|^2 + |A_L|^2} = \frac{A_{WP}A_{EM}^* + A_{EM}A_{WP}^*}{|A_{EM}|^2} \simeq \frac{G_F}{\frac{\alpha}{q^2}} \ . \tag{I.4}$$

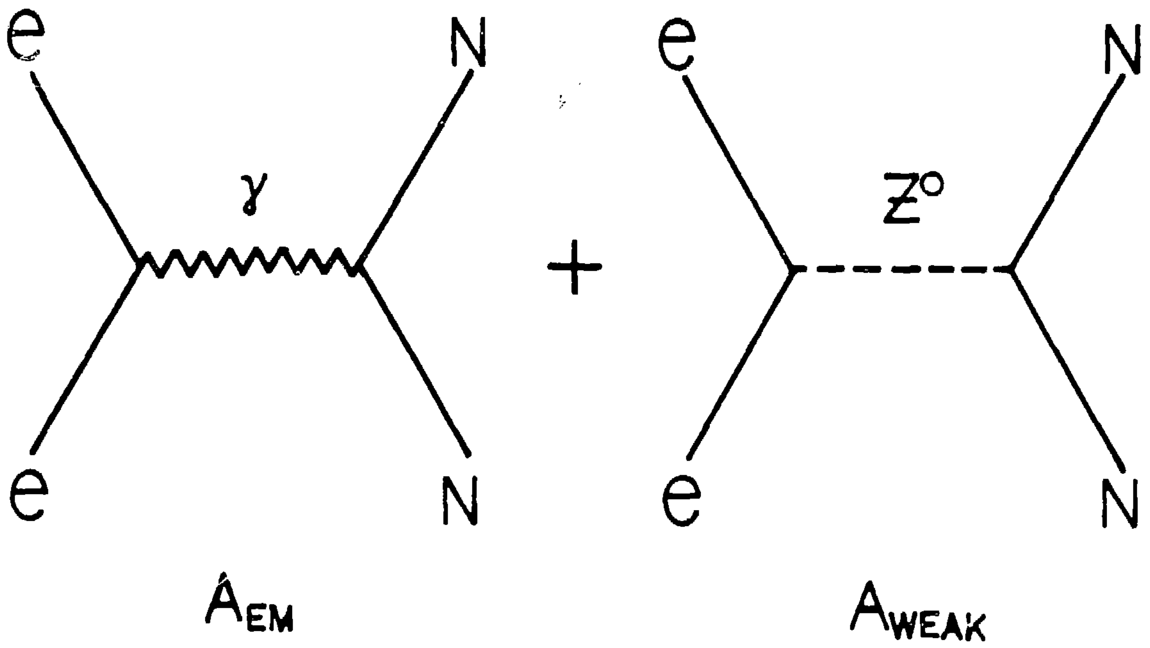

XBL 8511-4747

Fig. I-1. Diagram depicting photon (γ) and neutral vector boson (Z^0) exchange between an electron and a nucleon.

The size of the asymmetry can be estimated because $A_{EM} \approx \alpha/q^2$ and for a typical weak amplitude $A_{WP} = G_F$ where $G_F = 1.1663 \times 10^{-5}$ GeV$^{-2}c^4$, $\alpha = e^2/\hbar c$ = fine structure constant, and q = momentum transfer. This asymmetry is observable in high-energy deep-inelastic polarized electron scattering by nucleons and in low energy atomic spectroscopy.

The helicity-dependent asymmetry in the scattering of high energy electrons by a deuterium target was observed in an experiment performed at SLAC (Prescott 78,79). The handedness of the coordinate system is determined by the longitudinal polarization of the electron beam. The asymmetry was measured by observing the number of electrons scattered at a particular angle for both electron polarizations. At a momentum transfer of $q \approx 1$ GeV/c, the asymmetry predicted on the basis of the standard model, and actually obtained in the experiment, is $\delta \sim 10^{-4}$.

In low energy atomic physics, Z° exchange gives rise to a parity non-conserving term additional to the ordinary Coulomb interaction in the atomic Hamiltonian. This will induce a parity violating electric dipole amplitude between atomic states of the same nominal parity, which can be observed in optical transitions. Because the momentum transfer between an electron and a nucleon is quite small: $q \sim \alpha m_e$ in atoms, the asymmetry might be expected to be unobservable. However, there are some important enhancement factors which make it possible to observe the asymmetry in heavy atoms. One particular experiment in thallium is described in this chapter.

Experiments such as these put stringent and complementary constraints on the neutral weak coupling parameters. The results of these and other scattering experiments comprise a great deal of experimental evidence in support of the standard model. However, the most impressive evidence is contained in direct observations of the gauge bosons (W^+, W^-, Z°) that mediate the weak interaction (Arnison 83).

B. Parity Non-Conservation in Atoms

In atomic physics, a pseudoscalar Hamiltonian arises from Z° exchange between an electron and the atomic nucleus. Assuming the electron and nucleon neutral weak currents contain only vector and axial vector components, the currents take the form

$$J_e = V_e + A_e \qquad J_N = V_N + A_N \tag{I.5}$$

representing the sum of vector and axial vector parts. The weak amplitude can be written as a sum of scalar and pseudoscalar amplitudes:

$$J_e J_N = (V_e V_N + A_e A_N) + (A_e V_N + V_e A_N) \quad . \tag{I.6}$$

The scalar terms are unobservable, but the pseudoscalar terms can be observed through interference with an electromagnetic amplitude. The two pseudoscalar terms are

$$A_e V_N = \frac{G_F}{\sqrt{2}} \sum_i \bar{\Psi}_e \gamma_\lambda \gamma_5 \ {}_e(C_{1p}\ \bar{\Psi}_{pi} \gamma^\lambda \Psi_{pi} + C_{1n}\ \bar{\Psi}_{ni} \gamma^\lambda \Psi_{ni}) \tag{I.7}$$

and

$$V_e A_N = \frac{G_F}{\sqrt{2}} \sum_i \bar{\Psi}_e \gamma_\lambda \Psi_e (C_{2p}\ \bar{\Psi}_{pi} \gamma^\lambda \gamma_5 \Psi_{pi} + C_{2n}\ \bar{\Psi}_{ni} \gamma^\lambda \gamma_5 \Psi_{ni}) \tag{I.8}$$

where the sums are over all protons (p) and neutrons (n) in the nucleus. According to the standard model, the coupling constants are:

$$C_{1p} = \frac{1}{2}\,(1 - 4\sin^2\theta_W) \tag{I.9}$$

$$C_{1n} = -\frac{1}{2} \tag{I.10}$$

$$C_{2p} = g_A/2\ (1 - 4\sin^2\theta_W) \tag{I.11}$$

$$C_{2n} = -g_A/2\ (1 - 4\sin^2\theta_W) \tag{I.12}$$

where θ_W = the Weinberg angle and $g_A = 1.25$ is the axial vector coupling constant of β-decay. Assuming the standard model, the nonrelativistic reduction of the electronic and nucleonic currents illustrates the pseudoscalar nature of the effective atomic potentials induced by the terms A_eV_N and V_eA_N. We have

$$V_{PNC} = \frac{G_F}{4\sqrt{2}}\ \frac{1}{m_ec}Q_W\left\{\vec{\sigma}\cdot\vec{p}\ \delta^3(r) + \delta^3(r)\ \vec{\sigma}\cdot\vec{p}\right\} \tag{I.13}$$

and

$$V'_{PNC} = \frac{G_F}{4\sqrt{2}}\ \frac{1}{m_ec}(1 - 4\sin^2\theta_W)\ g_A\vec{\sigma}_N\cdot\vec{\sigma}\left\{\vec{\sigma}\cdot\vec{p}\ \delta^3(r) + \delta^3(r)\ \vec{\sigma}\cdot\vec{p}\right\} \tag{I.14}$$

for A_eV_N and V_eA_N, respectively, in the limit of a point nucleus. Here, $\frac{\vec{\sigma}}{2}$, $\vec{p}$, and $\vec{r}$ are the spin, momentum, and position of the electron, and $\vec{\sigma}_N$ is the nuclear spin operator. For a nucleus with Z protons and N neutrons, the weak charge is defined as

$$Q_W = (1 - 4\sin^2\theta_W)Z - N \quad , \tag{I.15}$$

and is roughly proportional to Z. The factors of Z and N appear in V_{PNC} because the nucleons add coherently over an electron de Broglie wavelength. In the case of V'_{PNC}, the nuclear spins appearing in σ_N cancel in pairs; the effects are of order Z^{-1} smaller than those of V_{PNC}, and are negligible in heavy atoms. The parity violating asymmetry is enhanced in heavy atoms by the approximately Z^3 dependence of V_{PNC} where two additional factors of Z come from the momentum of the electron at the nucleus and the density of the electron at the nucleus.

C. Parity Non-conservation in Atomic Thallium

The $6^2P_{1/2} \rightarrow 7^2P_{1/2}$ transition in atomic thallium has been studied extensively over the past decade because of its connection to the observation of parity non-conservation (Chu 77, Bucksbaum 81, Drell 84,85). This transition is nominally a forbidden magnetic dipole transition (with amplitude M), and is not allowed in the electric dipole approximation because the parity of the initial state $6^2P_{1/2}$ is the same as the final state $7^2P_{1/2}$. However, the effective pseudoscalar atomic potential V_{PNC} mixes $6^2P_{1/2}$ and $7^2P_{1/2}$ states with nearby $n^2S_{1/2}$ states of opposite parity.

$$|6^2P_{1/2}\rangle \rightarrow |6^2P_{1/2}\rangle + \sum_{nS_{1/2}} \frac{|nS_{1/2}\rangle\langle nS_{1/2}|V_{PNC}|6^2P_{1/2}\rangle}{E_{6P} - E_{nS}} \qquad (I.16)$$

$$|7^2P_{1/2}\rangle \rightarrow |7^2P_{1/2}\rangle + \sum_{nS_{1/2}} \frac{|nS_{1/2}\rangle\langle nS_{1/2}|V_{PNC}|7^2P_{1/2}\rangle}{E_{7P} - E_{nS}} \qquad (I.17)$$

Thus, V_{PNC} induces a parity violating electric dipole amplitude between states of the same nominal parity. To first order in V_{PNC},

$$\mathcal{E}_P = \sum_{nS_{1/2}} \frac{\langle 7P_{1/2}|E1|nS_{1/2}\rangle\langle nS_{1/2}|V_{PNC}|6P_{1/2}\rangle}{E_{6P} - E_{nS}} + \frac{\langle 7P_{1/2}|V_{PNC}|nS_{1/2}\rangle\langle nS_{1/2}|E1|6P_{1/2}\rangle}{E_{7P} - E_{nS}} \quad . \qquad (I.18)$$

In an experiment performed by P.S. Drell and E.D. Commins (Drell 84,85), the interference between a Stark induced electric dipole amplitude βE (described in the next chapter) and the parity non-conserving electric dipole amplitude $\mathcal{E}_P$ was observed. The $6^2P_{1/2} \rightarrow 7^2P_{1/2}$ (293 nm) transition was excited with linearly polarized laser light passing through ^{205}Tl vapor in the presence of crossed electric and magnetic fields (see Fig. I-2). The transition probability contains a pseudoscalar interference term proportional to

$$\hat{\varepsilon}\cdot\vec{B}\;\hat{\varepsilon}\cdot\vec{E}\times\vec{B}$$

where $\hat{\varepsilon}$ is the laser polarization. The magnetic field $\vec{B}$ was used to split the Zeeman components of the hyperfine structure in the transition, and the electric field $\vec{E}$ was used to induce the Stark effect. In particular for a $\Delta m_F=0$ transition, the transition probability is proportional to

$$T_{\Delta m_F=0} \propto \left[\beta^2 E^2 \sin^2\theta - 2\beta E\,\mathrm{Im}\,\mathcal{E}_P \sin\theta \cos\theta\right] \quad . \qquad (I.19)$$

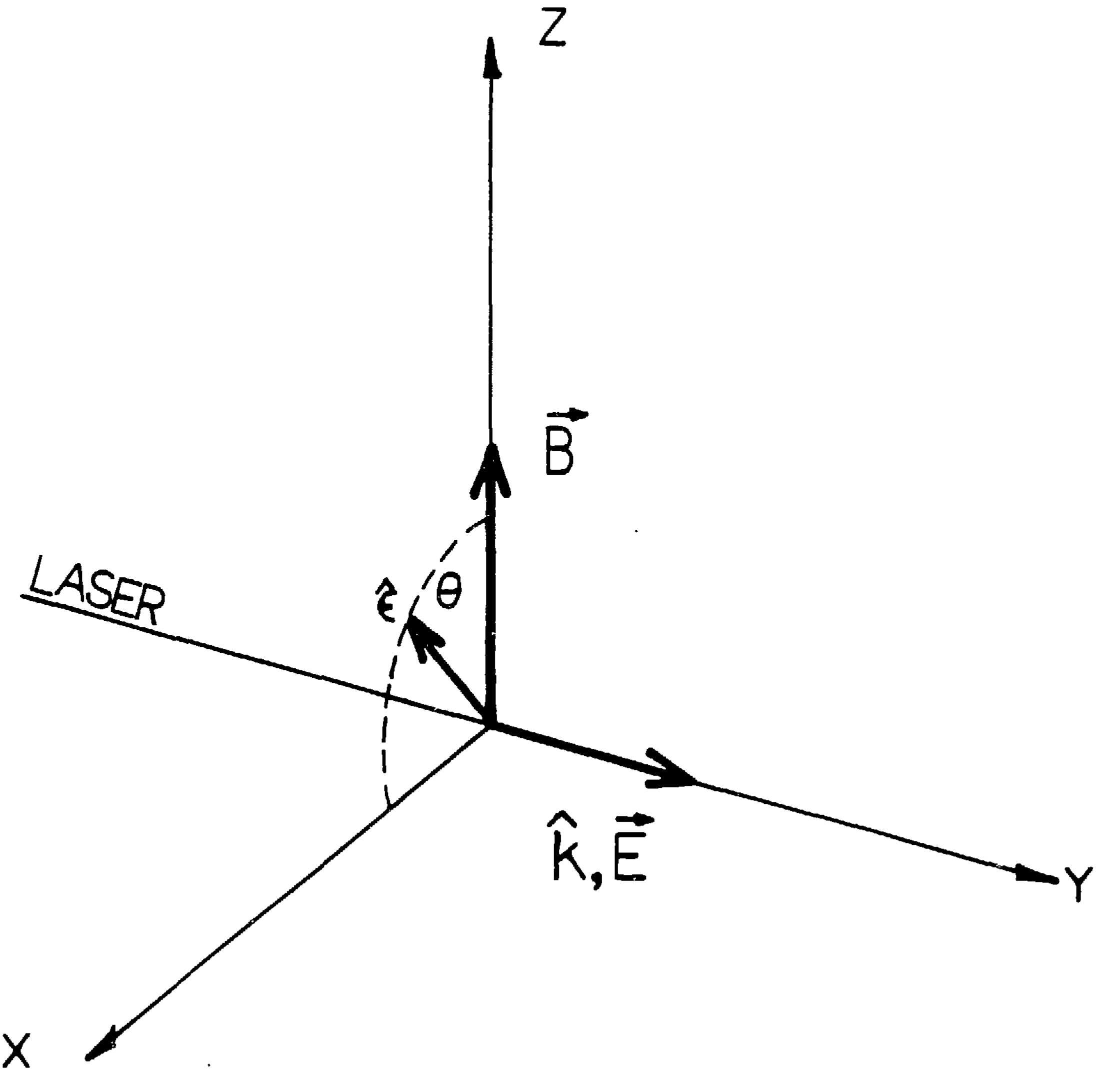

XBL 8511-4748

Fig. I-2. Coordinate system for the parity violating-Stark E1 interference experiment showing relative orientation of the laser beam, photon polarization, magnetic and electric fields.

For the relative orientation of $\hat{\varepsilon}$ and $\vec{E}$ chosen, the magnetic dipole and Stark induced electric dipole amplitudes do not interfere. The interference between $\mathcal{E}_p$ and βE is observed by measuring an asymmetry in the intensity of $7^2P_{1/2} \rightarrow 6^2P_{3/2}$ (535 nm) decay fluorescence when $\vec{E}$ or θ is reversed.

$$\delta = \frac{T_+ - T_-}{T_+ + T_-} = -\,\mathrm{Im}\,\frac{2\,\mathcal{E}_P}{\beta E}\cot\theta \quad . \qquad (\Delta m_F=0) \qquad (I.20)$$

In this way, an experimental value for the ratio

$$\mathrm{Im}\,\frac{\mathcal{E}_P}{\beta} = -\,1.73 \pm 0.26 \pm 0.07 \text{ mV/cm} \qquad (I.21)$$

was obtained where the first and second uncertainties are statistical and systematic, respectively. However, one would like to know the parity nonconserving electric dipole amplitude $\mathcal{E}_p$ independent of the Stark amplitude coefficient β because $\mathcal{E}_p$ contains information about the effects of neutral currents in atoms. A direct measurement of β allows us to determine $\mathcal{E}_p$, which can be compared with theoretical estimates based on the standard model of electroweak interactions.

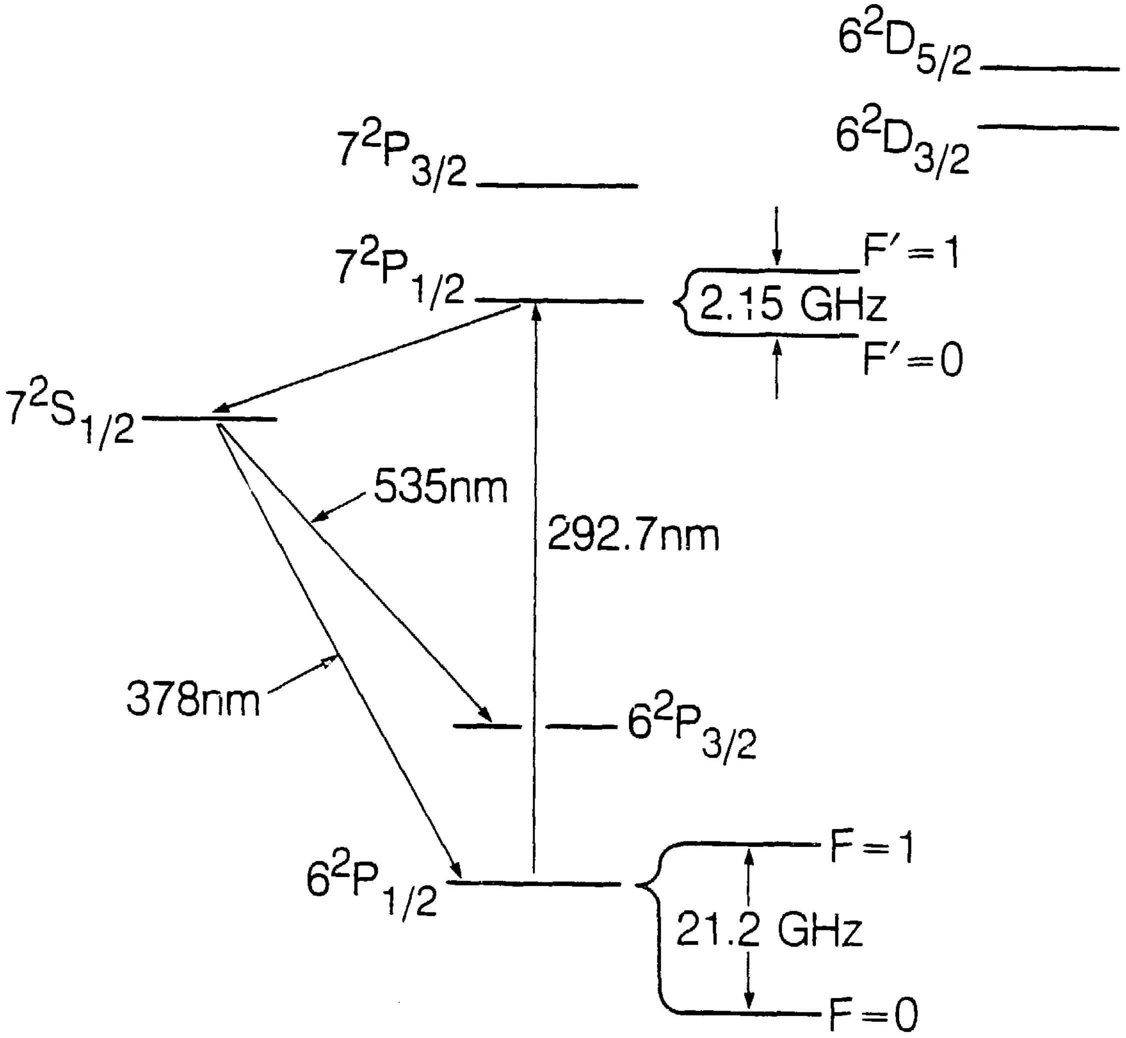

XBL 859-3970

Fig. I-3. Low lying energy levels of Tl (not to scale). The hyperfine components of the $6^2P_{1/2}$ and $7^2P_{1/2}$ states are shown.

II. THE STARK EFFECT

A. Theory: Stark Amplitude Coefficients

This thesis describes the measurement of Stark induced electric dipole transition amplitudes from the ground state of neutral thallium $6^2P_{1/2}$ to the $7^2P_{1/2}$ state. This transition is not allowed in the electric dipole approximation. However, when an electric field is externally applied to the atoms, an electric dipole (E1) transition can occur. The electric field mixes the $6^2P_{1/2}$ and $7^2P_{1/2}$ states with nearby $n^2S_{1/2}$ and $n^2D_{3/2}$ states, inducing an E1 transition amplitude. In first order perturbation theory, the mixed states can be written

$$\overline{|6^2P_{1/2}>} \simeq |6^2P_{1/2}> + \sum_{\substack{nS_{1/2}\\ nD_{3/2}}} \frac{|n><n|H_{STARK}|6^2P_{1/2}>}{E_{6P} - E_n} \qquad \text{(II.1)}$$

$$\overline{|7^2P_{1/2}>} \simeq |7^2P_{1/2}> + \sum_{\substack{nS_{1/2}\\ nD_{3/2}}} \frac{|n><n|H_{STARK}|7^2P_{1/2}>}{E_{7P} - E_n} \qquad \text{(II.2)}$$

where $H_{STARK} = e\vec{E}\cdot\vec{r}$ is the Hamiltonian describing the interaction of the valence electron with the external electric field. The electric dipole amplitude between the mixed states is then

$$\langle\overline{7^2P_{1/2}}\,|\,E1\,|\,\overline{6^2P_{1/2}}\rangle = \sum_{\substack{nS_{1/2}\\ nD_{3/2}}} \frac{\langle 7^2P_{1/2}|E1\ n\rangle\langle n|H_{STARK}|6^2P_{1/2}\rangle}{E_{6P}-E_n}$$

$$+\sum_{\substack{nS_{1/2}\\ nD_{3/2}}} \frac{\langle 7^2P_{1/2}|H_{STARK}|n\rangle\langle n|E1|6^2P_{1/2}\rangle}{E_{7P}-E_n}\ . \qquad (II.3)$$

When linear polarization is chosen as the basis to describe the electromagnetic radiation, the Stark induced electric dipole amplitude can be expressed simply in terms of two different matrix elements,

$$\langle\overline{7^2P_{1/2}\ m_J}|e\hat{\epsilon}\cdot\vec{r}|\overline{6^2P_{1/2}\ m_J}\rangle = \alpha E \qquad (\hat{\epsilon}\parallel\vec{E}) \qquad (II.4)$$

and

$$\langle\overline{7^2P_{1/2}\ m_J\pm1}|e\hat{\epsilon}\cdot\vec{r}|\overline{6^2P_{1/2}\ m_J}\rangle = i\beta E \qquad (\hat{\epsilon}\cdot\vec{E})\ . \qquad (II.5)$$

The Stark induced electric dipole amplitude is proportional to the coefficient α when the linear polarization of the light, $\hat{\epsilon}$, is parallel to the electric field $(\hat{\epsilon}\parallel\vec{E})$, and is proportional to the coefficient β when ϵ is perpendicular to $\vec{E}$ $(\hat{\epsilon}\perp\vec{E})$. In the one-electron central-field approximation, these quantities are given in lowest order by:

$$\alpha = \frac{e^2}{9} \sum_{nS_{1/2}} R_{7P,nS}\, R_{6P,nS} \left[\frac{1}{E_{7P} - E_{nS}} + \frac{1}{E_{6P} - E_{nS}} \right]$$

$$+ \frac{2e^2}{9} \sum_{nD_{3/2}} R_{7P,nD}\, R_{6P,nD} \left[\frac{1}{E_{7P} - E_{nD}} + \frac{1}{E_{6P} - E_{nD}} \right] \qquad \text{(II.6)}$$

and

$$\beta = \frac{e^2}{9} \sum_{nS_{1/2}} R_{7P,nS}\, R_{6P,nS} \left[\frac{1}{E_{6P} - E_{nS}} - \frac{1}{E_{7P} - E_{nS}} \right]$$

$$+ \frac{e^2}{9} \sum_{nD_{3/2}} R_{7P,nD}\, R_{6P,nD} \left[\frac{1}{E_{7P} - E_{nD}} - \frac{1}{E_{6P} - E_{nS}} \right] \qquad \text{(II.7)}$$

where $E_{6P} = E(6^2P_{1/2})$, $E_{7P} = E(7^2P_{1/2})$, etc., and

$$R_{7P,nS} = \int_0^\infty \psi_{7^2P_{1/2}}(r)\, \psi_{n^2S_{1/2}}(r)\, r^3 dr \quad ,$$

etc., are radial matrix elements.

The Stark coefficients were calculated by Neuffer and Commins using wavefunctions generated as solutions to the Dirac equation in a modified Tietz central potential. The quantities α and β were evaluated using a Green function technique, which includes a sum over all discrete and continuous S and D states yielding (Neuffer 77)

$$\alpha_0 = 2.05 \times 10^{-5}\ \mu_0\ \text{cm/V}$$

$$\beta_0 = 1.64 \times 10^{-5}\ \mu_0\ \text{cm/V} \qquad \text{(II.8)}$$

$$\frac{\beta_0}{\alpha_0} = 0.80 \quad .$$

The theoretical uncertainty in α_0 and β_0 is estimated to be about 20% based on comparisons of calculated electric dipole matrix elements with experimental values. However, the model assumes a one-electron central-field, and does not account for the effects of the electric field on the core electrons. Screening of the electric field by the core electrons is expected to have a large systematic effect on the Stark coefficients, and this is not taken into account by this naive model. The ratio $\frac{\beta}{\alpha}$ has been measured (Chu 77) to be

$$\frac{\beta}{\alpha} = 0.84 \pm 0.05 \tag{II.9}$$

in agreement with the theoretical prediction. In the next section, we present a description of the method used to measure α and β.

B. Method of Measuring α and β

In the present experiment, the Stark coefficient α is determined by absorption. Linearly polarized laser light tuned to the $6^2P_{1/2} \rightarrow 7^2P_{1/2}$ (293 nm) resonance is absorbed as it passes through thallium vapor in the presence of an externally applied electric field. For $E \gg 1$ V/cm, the Stark E1 contribution (II.4) greatly dominates over M (see appendix) and $\mathcal{E}_p$ and the latter amplitudes may be neglected. The coordinate system chosen for the experiment is illustrated in Figure II-1 where $\hat{\epsilon}$ is the laser polarization, $\vec{E}$ is the electric field, and $\hat{k}$ is the propagation direction of the light.

The hyperfine structure of the transition is resolved, and each hyperfine component has a slightly different amplitude where the

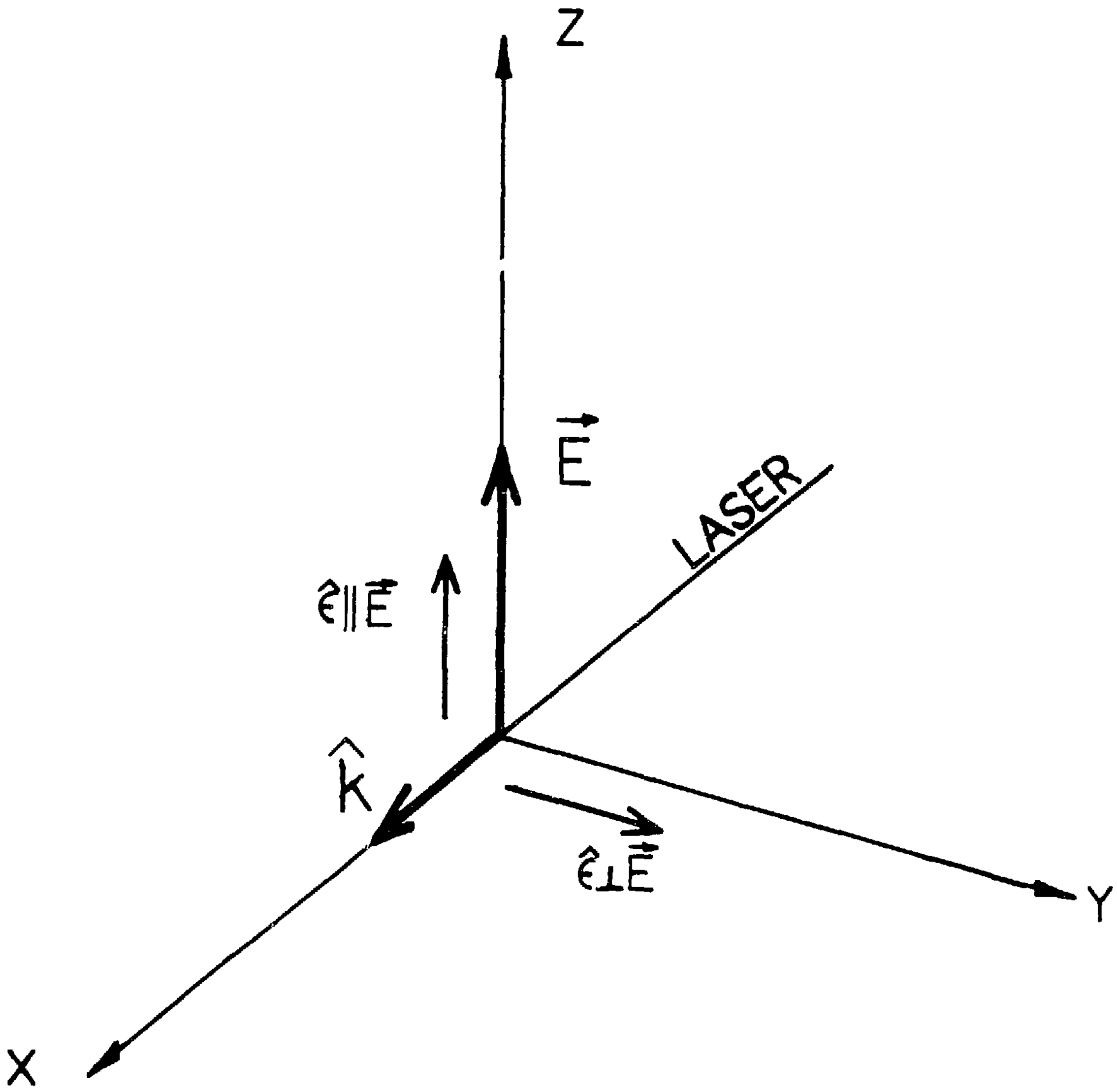

XBL 8511-4749

Fig. II-1. Coordinate system for the experiment showing relative orientation of the laser beam, photon polarization, and electric field.

nuclear spin of ^{205}Tl is 1/2. The transition amplitudes are shown in Figure II-2, and the transition probabilities for the various hyperfine components are proportional to the values in the following tabulation:

$(6^2P_{1/2})\ F \rightarrow (7^2P_{1/2})\ F'$ TRANSITION	TRANS. PROB.
$0 \rightarrow 0 \quad (\hat{\varepsilon} \parallel \vec{E})$	α^2E^2
$0 \rightarrow 1 \quad (\hat{\varepsilon} \perp \vec{E})$	β^2E^2
$1 \rightarrow 0 \quad (\hat{\varepsilon} \perp \vec{E})$	β^2E^2
$1 \rightarrow 1 \quad (\hat{\varepsilon} \parallel \vec{E})$	$3\alpha^2E^2$
$1 \rightarrow 1 \quad (\hat{\varepsilon} \perp \vec{E})$	$2\beta^2E^2$

(II.10)

The Stark coefficient α is determined by measuring the absorption of a linear polarized laser beam tuned to the F=1 → F'=1 resonance when the beam passes through a cell containing ^{205}Tl vapor at known temperature T, in known electric field $\vec{E} \parallel \hat{\varepsilon}$, over a region of known length . The intensity of the emerging beam, I, may be expressed in terms that of the entering beam, I_0, by $I = I_0 \exp(-\mu\ell)$ where

$$\mu(\nu) = \frac{(2\pi)^2}{\hbar c}\,\frac{n}{4}(3\alpha^2E^2)\left(\frac{mc^2}{2\pi kT}\right)^{1/2} \exp -\left[\frac{m\lambda_0^2}{2kT}(\nu-\nu_0)^2\right] \qquad \text{(II.11)}$$

is the absorption coefficient. Here, n is the density of $6^2P_{1/2}$ atoms in cm^{-3}, m is the mass of a ^{205}Tl atom in grams, T is the effective vapor temperature in Kelvin, λ_0 = 292.7 nm, and ν, ν_0 are the photon and resonance frequencies, respectively. Equation (II.11) is valid provided the laser bandwidth is much less than the Doppler width due

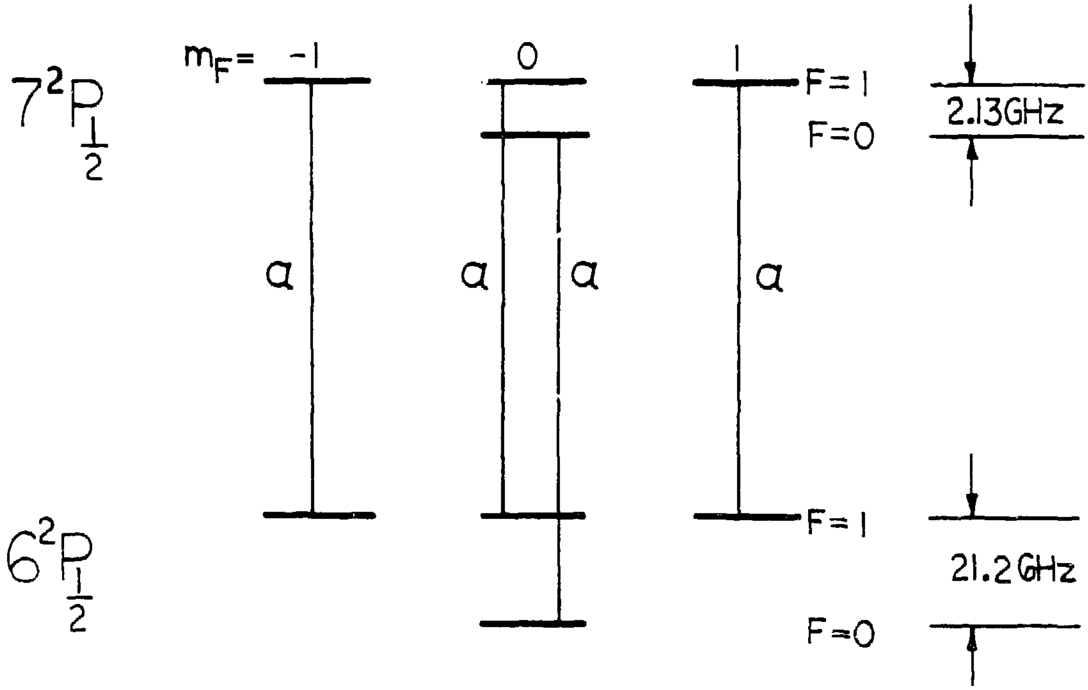

Fig. II-2a. Stark E1 matrix elements for photon polarization $\hat{\varepsilon}$ parallel to $\vec{E}$.

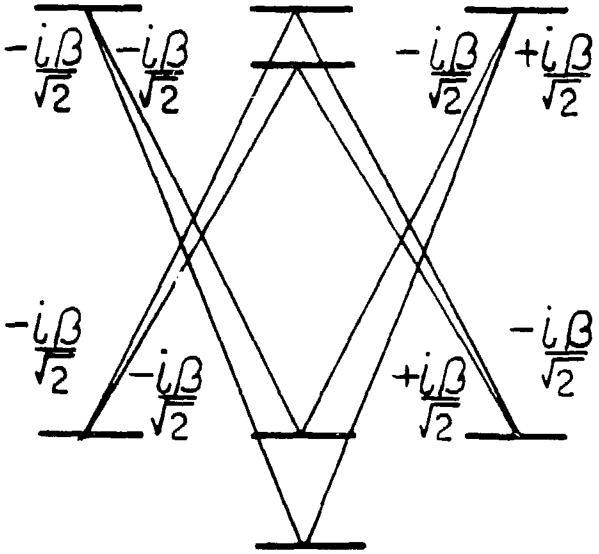

XBL 8511-4750

Fig. II-2b. Stark E1 matrix elements for photon polarization $\hat{\varepsilon}$ perpendicular to $\vec{E}$.

to thermal motion of the atoms along the direction of the beam, a condition very well satisfied here. (The correction to (II.11) for finite laser band width is less than 0.5%, and may be neglected.) The density, n, as determined from published values of thallium vapor pressure is uncertain to 20%. Before α can be precisely determined from a measurement of μ, the density must be calibrated.

This is done by measuring absorption in an allowed E1 transition with known oscillator strength. The absorption of a laser beam tuned to $6^2P_{3/2}F=1 \rightarrow 7^2S_{1/2}F'=0$ (535 nm) transition is measured in the same cell under identical conditions. For sufficiently weak intensities (such that stimulated emission effects may be neglected), this absorption is described by $I'=I_0'\exp(-\mu'\ell')$ where ℓ' is the length of the cell, and

$$\mu'(\nu) = \frac{n}{4}\, e^{-\frac{\Delta E}{kT}}\, A(7^2S_{1/2} \rightarrow 6^2P_{3/2})\, \frac{\lambda'^3}{8\pi c} \left(\frac{mc^2}{2\pi kT}\right)^{1/2} \exp\left[\frac{-m\lambda'^2}{2kT}(\nu-\nu')^2\right] . \tag{II.12}$$

Here, $A(7^2S_{1/2} \rightarrow 6^2P_{3/2}) = (7.11 \pm 0.16)\times10^7\ \mathrm{sec}^{-1}$ is the precisely determined coefficient for spontaneous emission (Hsieh 72) in $7^2S_{1/2} \rightarrow 6^2P_{3/2}$, and ν' is the resonance frequency for $\lambda' = 535$ nm. The density of $6^2P_{3/2}$ atoms is related to the density, n, of $6^2P_{1/2}$ atoms by a Boltzmann factor, $e^{-\Delta E/kT}$, accounting for the energy difference $E(6^2P_{3/2}) - E(6^2P_{1/2}) = \Delta E = 7793\ \mathrm{cm}^{-1}$.

In the ratio of the absorption coefficients,

$$\frac{\mu(\nu_0)}{\mu'(\nu')} = \frac{\frac{(2\pi)^2}{\hbar c}\,(3\alpha^2E^2)}{e^{\frac{-\Delta E}{kT}}\,A(7^2S_{1/2} \to 6^2P_{1/2})\,\frac{\lambda'^3}{8\pi c}} \tag{II.13}$$

the factors of n and $T^{-1/2}$ cancel. (The exponential factors involving $(\nu-\nu_0)$ and $(\nu-\nu')$ are set equal to one on resonance.) However, T must still be known because of the Boltzmann factor. Once α is found from II.13, β is determined by measuring the ratio of intensities β^2/α^2 in decay fluorescence of $7^2S_{1/2} \to 6^2P_{3/2}$ (535 nm) while driving the $6^2P_{1/2} \to 7^2P_{1/2}$: $0 \to 1$ and $0 \to 0$ resonances (see II.10).

In order to test the system, absorption is also observed in another allowed E1 transition $6^2P_{3/2} \to 7^2D_{5/2}$ (291.8 nm), with known oscillator strength. This absorption coefficient is measured in the same cell under identical conditions. In this transition, the hyperfine structure of the $7^2D_{5/2}$ state is not resolved, and the hyperfine structure of the $6^2P_{3/2}$ state is only partially resolved where the Doppler profile of the F=1 and F=2 transitions overlap.

$$\mu''(\nu) = 3n\,e^{\frac{-\Delta E}{kT}}\,A(7^2D_{5/2} \to 6^2P_{3/2})\,\frac{\lambda''^3}{8\pi c}\left(\frac{mc^2}{2\pi kT}\right)^{1/2} \times \left\{\frac{3}{8}\exp\frac{-m\lambda''^2}{2kT}(\nu-\nu_1)^2 + \frac{5}{8}\exp\frac{-m\lambda''^2}{2kT}(\nu-\nu_2)^2\right\} . \tag{II.14}$$

Here, ν_1 and ν_2 are the resonance frequencies for the $6^2P_{3/2}$ F=1, F=2 $\to 7^2D_{5/2}$ transitions, respectively, and λ'' = 291.8 nm. The peak value of the absorption coefficient is

$$\mu''(\nu_{peak}) = 3n\ e^{\frac{-\Delta E}{kT}}\ A(7^2D_{5/2} \rightarrow 6^2P_{3/2})\ \frac{\lambda''^3}{8\pi c}\left(\frac{mc^2}{2\pi kT}\right)^{1/2}\ \left\{0.936\right\} \qquad \text{(II.15)}$$

evaluated for the operating temperature 1030K, and using $\nu_2-\nu_1 = 0.525$ GHZ. The system is tested by comparing the coefficient for spontaneous emission in $7^2D_{5/2} \rightarrow 6^2P_{3/2}$ as determined from the measurement of $\mu''(\nu_{peak})$ with the known value (Gallagher 64)

$$A(7^2D_{5/2} \rightarrow 6^2P_{3/2}) = (4.2 \pm 0.5)\text{x}10^7\ \text{sec}^{-1}. \qquad \text{(II.16)}$$

III. APPARATUS

An overview of the apparatus is shown in Figure III-1, and the experiment is illustrated schematically in Figure III-2. In this chapter, the individual components are described in detail.

A. Thallium Cell and Ovens

In order to produce a measurable absorption due to the Stark effect in the $6^2P_{1/2} \rightarrow 7^2P_{1/2}$ transition, thallium vapor must be present at a density of $\sim 10^{15}$ atoms/cc. This density occurs at a vapor pressure of ~0.1 torr when thallium is heated to ~1000K (Nesmayonov 63). To satisfy these requirements, the thallium is placed in a cell of fused-silica surrounded by stainless steel ovens. Fused-silica is ideally suited for this purpose because it is transparent at 293 nm and 535 nm, and is only very slightly reactive with thallium at high temperatures. The ovens are surrounded by a rough vacuum tank.

The cell is shown in Figure III-3. The main body of the cell is a fused-silica cylinder of length, $\ell' = 25$ cm, 22 mm O.D., and 1 mm walls. A $3\frac{1}{2}$ in. stem appended to the bottom of the cell contains the thallium reservoir. The interior of the cell is connected to a Vacion pump (Varian) through a vacuum pipe, but is isolated from the pump by a ground quartz ball valve while taking data. The valve can be remotely opened to remove impurities. The cell hangs by the vacuum pipe from the top of the rough vacuum tank. The windows of the cell, through which the laser beam passes, are 1/8 in. thick Suprasil quartz disks (Amersil), which are slightly canted to avoid unwanted reflections.

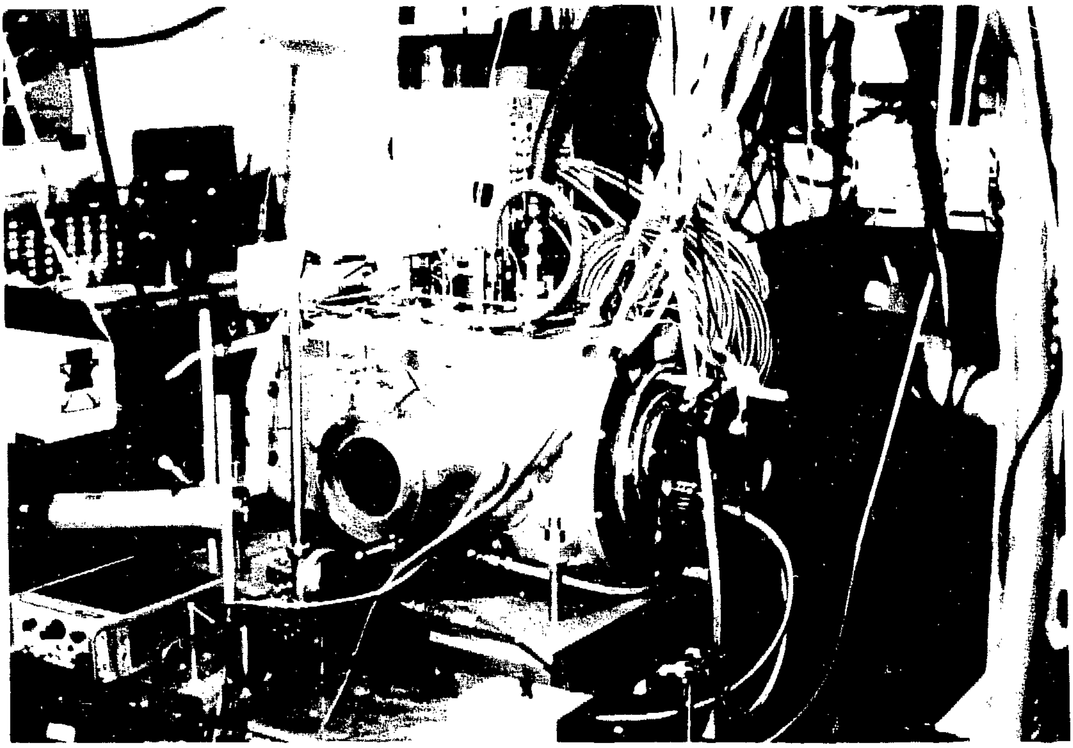

CBB 859-7545

Fig. III-1. Overview of experimental apparatus showing vacuum tank with normalization detector in the foreground. In the side of the vacuum tank is a port for viewing fluorescence. Above, the electric field pulser is visible.

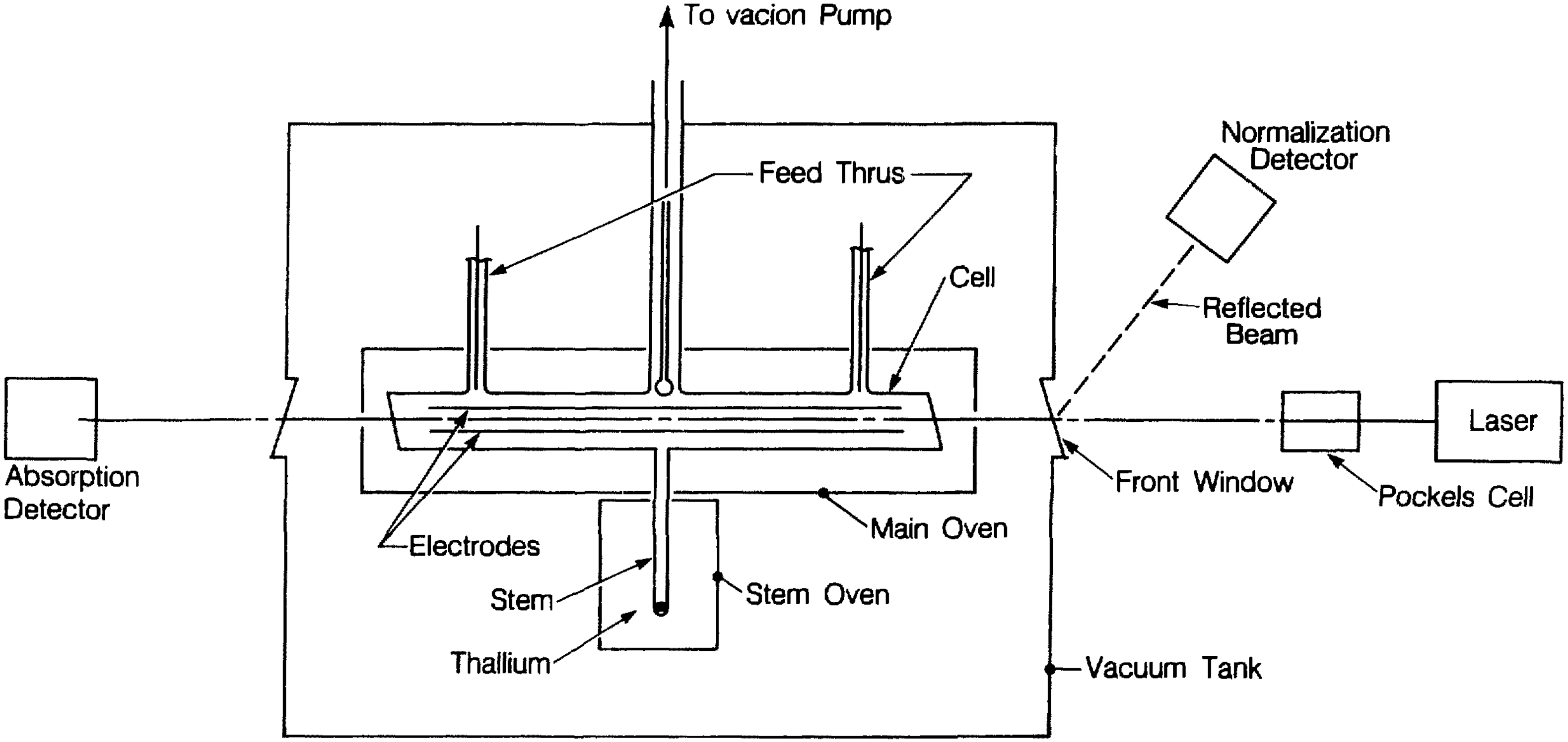

XBL 859-3968

Fig. III-2. Schematic diagram of the experimental apparatus.

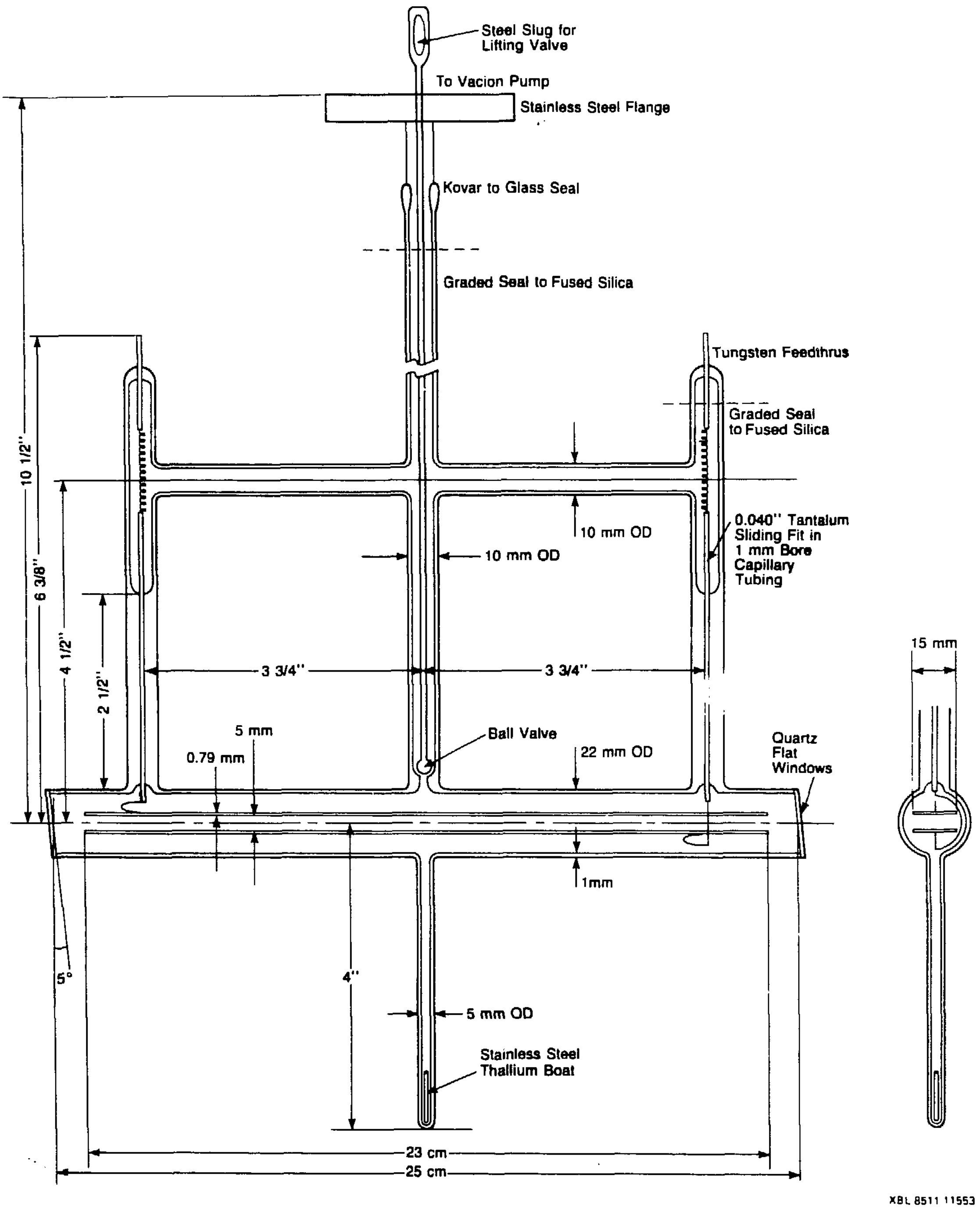

Fig. III-3. Diagram showing the actual dimensions of the cell.

The cell contains a pair of metal electrodes, which provide the electric field necessary to produce the Stark effect. These electrodes are flat polished stainless steel plates of length ℓ = 23 cm, width 1.5 cm, and thickness 0.79 mm. Before being installed, the electrodes were thoroughly cleaned and etched with acid to remove impurities, which might react with quartz at high temperatures, and reduce the optical quality of the cell. The electrodes are held parallel with a separation of 0.497 ± 0.001 cm by electroformed fused-silica spacers. Connections from the electrodes to the outside are made by tantalum wires attached to tungsten feedthrus. Figure III-4 shows the electrodes and spacers.

The main body of the cell is surrounded by a stainless steel rectangular oven (see Figure III-5). This main oven (shown in Figure III-6) is divided in half by a vertical plane along its length and consists of two pieces. There are 3/8 in. diameter laser entrance and exit holes at each end, and a 1/2 in. diameter port for viewing fluorescence in one side. These openings were made as small as conveniently possible to reduce the temperature gradients along the path of the laser beam. The heating elements, made from nichrome wire, are wound around both pieces of the oven, and are electrically insulated with ceramic spacers. The heaters run at 5 amp a.c. in series with a total resistance of 36Ω. A 3-layer stainless steel heat shield surrounds the main oven to reduce radiative heat loss. The operating temperature of the main oven is 1030K, measured with three chromel-alumel thermocouples (CRC).

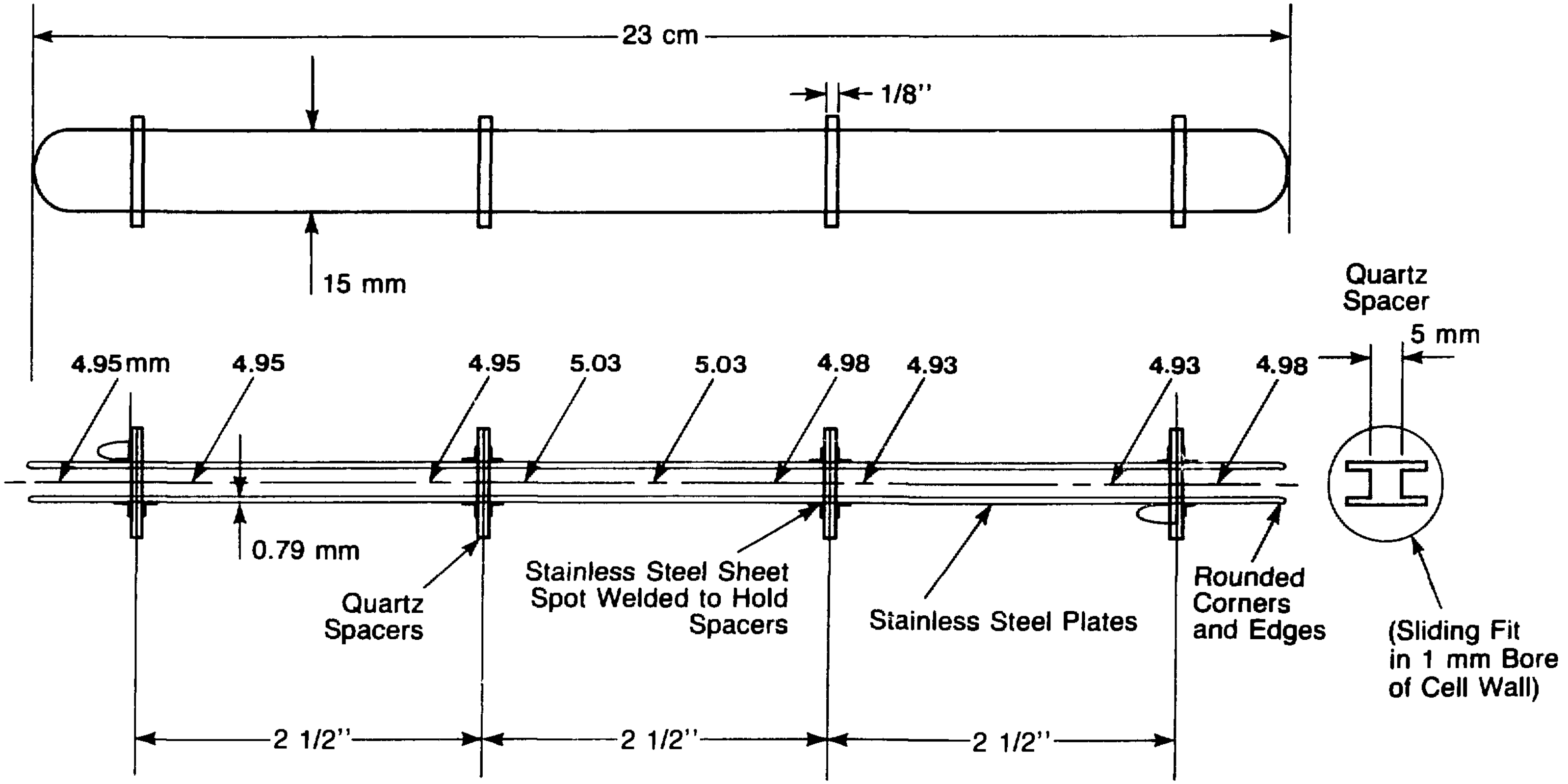

XBL 8511-11550

Fig. III-4. Diagram showing electric field plates and precision ground spacers. The spacing of the plates was accurately measured at several positions along their length before installation in the cell.

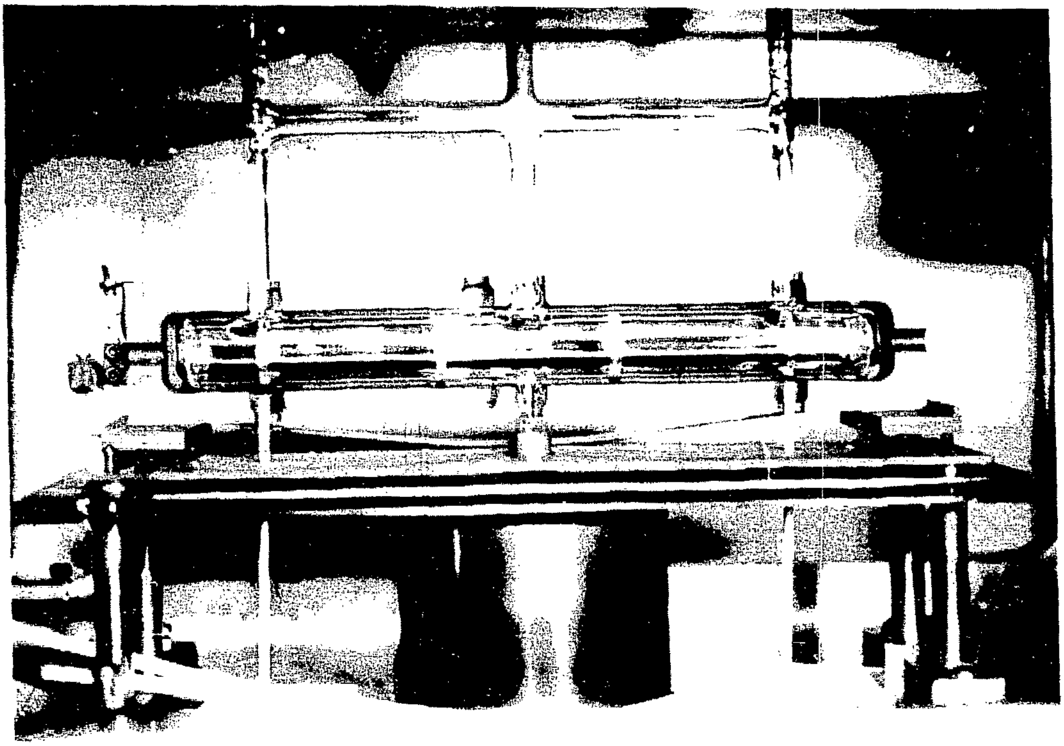

CBB 859-7553

Fig. III-5. Thallium cell with one piece of the main oven in place. The electric field plates and feed throughs are visible. In the center is the vacuum pipe and ball valve. The stem extends down into the stem oven which is surrounded by a heat shield. Laser entrance and exit ports are visible at each end of the main oven. Two thermocouples pass through ports in the bottom of the oven.

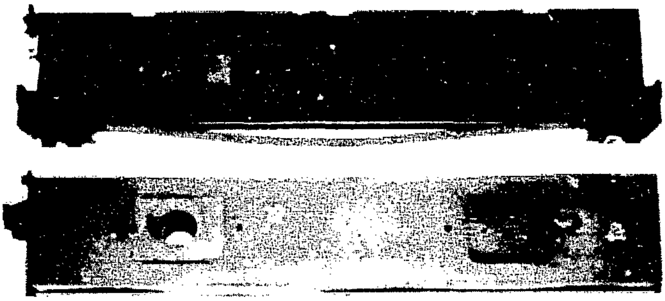

CBB 859-7557

Fig. III-6. Main oven showing port for viewing fluorescence in one side. A third thermocouple (measuring T_{main}) is placed in the hole at the center of the oven wall.

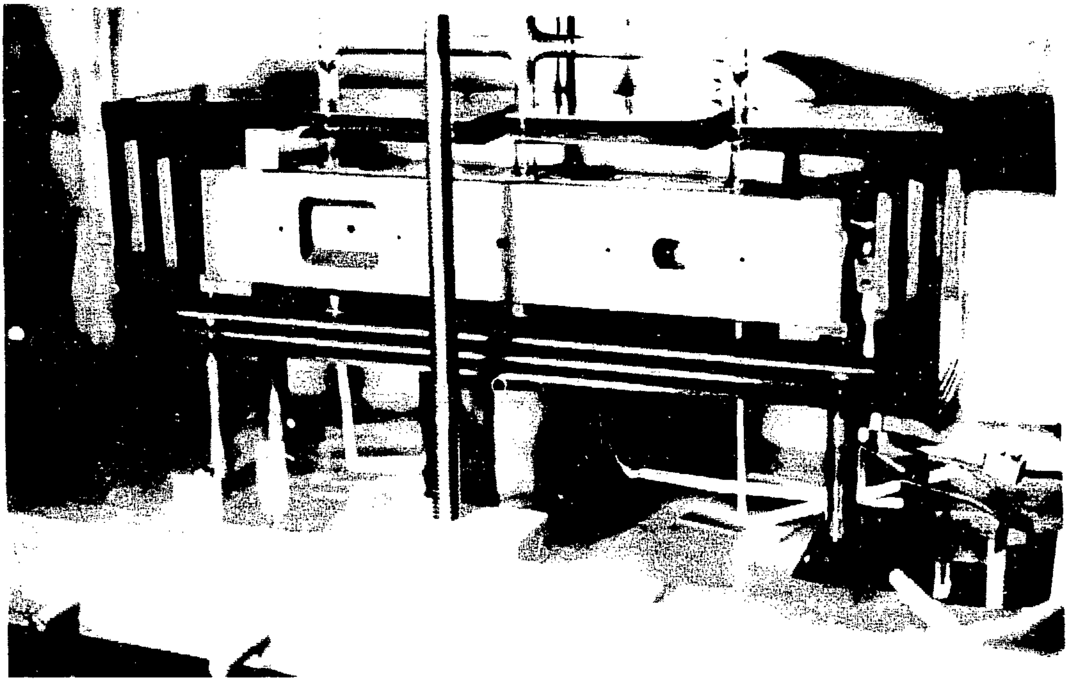

CBB 859-7549

Fig. III-7. Main oven completely assembled and surrounded by three layers of partially assembled heat shields.

The stem extends through the bottom of the main oven into a separate stainless steel stem oven (see Figure III-8) surrounded by one layer of heat shield. The heating elements are also made from nichrome wire, and run at 3.2 amp a.c. with a resistance of 18Ω. Under operating conditions, the stem is kept 70° cooler than the main oven, thus allowing thallium to condense only in the reservoir and not in the main body of the cell. The temperature of the stem oven is measured with a chromel-alumel thermocouple.

The ovens are enclosed in a rough vacuum tank where a pressure of 20 μ is maintained by a mechanical pump. The vacuum reduces stress on the cell, and keeps impurities from diffusing into the cell walls at high temperatures. The stainless steel ovens and nichrome heaters are allowed to oxidize in the rough vacuum to prevent them from reducing at elevated temperatures. The vacuum also prevents convective heat loss by the ovens.

Both ovens are powered with a.c. line voltage through a Sola constant voltage transformer, which removes variations in power due to fluctuations in line voltage. A separate variac controls the power supplied to each oven from the transformer, and provides a means of independently adjusting the temperatures. Using this method, the temperatures of both ovens can be reliably reproduced from day to day.

When the cell was installed, it was initially evacuated using a sorption pump. As the pressure dropped below 10^{-4} torr, the Vacion pump was started and used exclusively to maintain a pressure $<10^{-8}$ torr. The cell was then baked out by heating up the main oven to operating temperature. Thallium compounds and other impurities

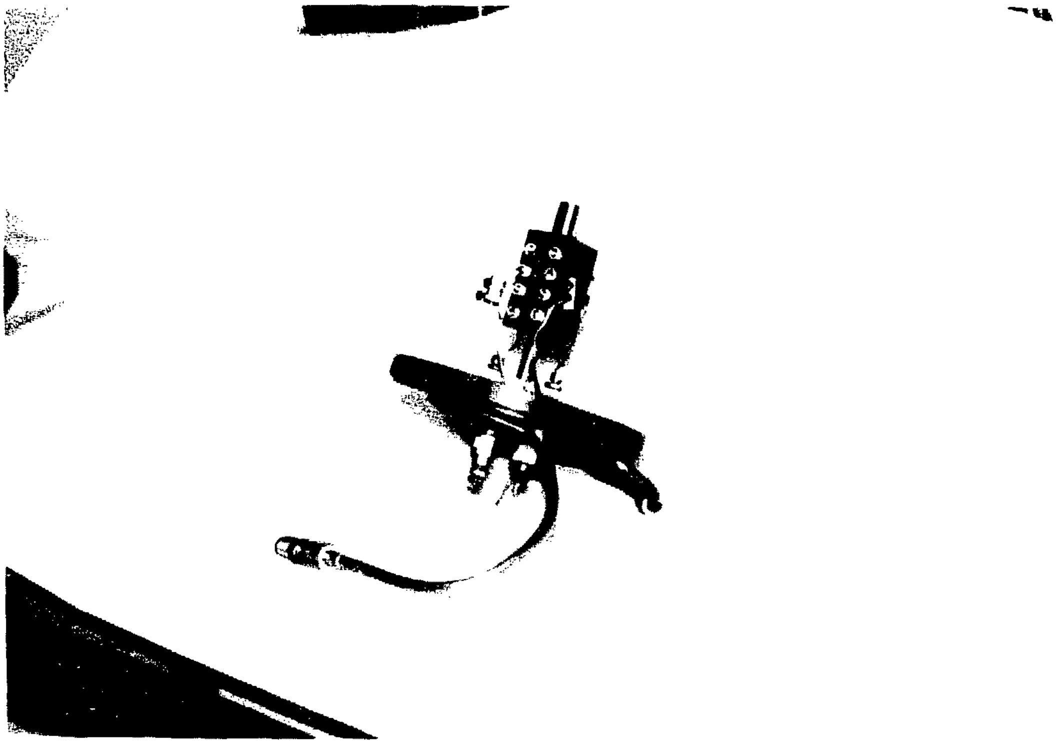

CBB 859-7543

Fig. III-8. Stem oven mounted on water cooled vacuum flange.

were removed by heating the stem oven to operating temperature, and opening the ball valve momentarily to purge the cell. Normally, the valve remains closed while the stem is hot to avoid losing thallium.

1. Temperature Measurements

The temperature of the main oven is very important, and must be determined accurately because it enters into the Boltzmann factor, $e^{-\Delta E/kT}$ (where $\Delta E = E(6^2P_{3/2}) - E(6^2P_{1/2})$), for the $6^2P_{3/2}$ population in the density calibration. Under normal operating conditions, the main oven temperature is measured often in three locations with chromel-alumel thermocouples all referenced to 0°C. However, temperature gradients along the path of the laser beam also affect the Boltzmann factor. These gradients arise from the beam end holes, small ports for the stem, fluorescence detection, feedthrus, and thermocouples. Before the thallium cell was installed, many preliminary temperature determinations, made with a moveable axial thermocouple, lead to the final choice of oven ports designed to minimize temperature variations. The final temperature profile at a typical operating temperature is shown in Figure III-9. With a known temperature profile, one can define a correction factor C for small variations in temperature

$$\int_0^{\ell'} e^{-\frac{\Delta E}{kT(x)}}\,dx \approx \sum_i e^{\frac{-\Delta E}{kT_i}}\,\Delta\ell_i' \equiv C\ell' e^{-\frac{\Delta E}{kT_{main}}} \qquad \text{(III.1)}$$

where T_{main} is the temperature deep inside the wall of the main oven.

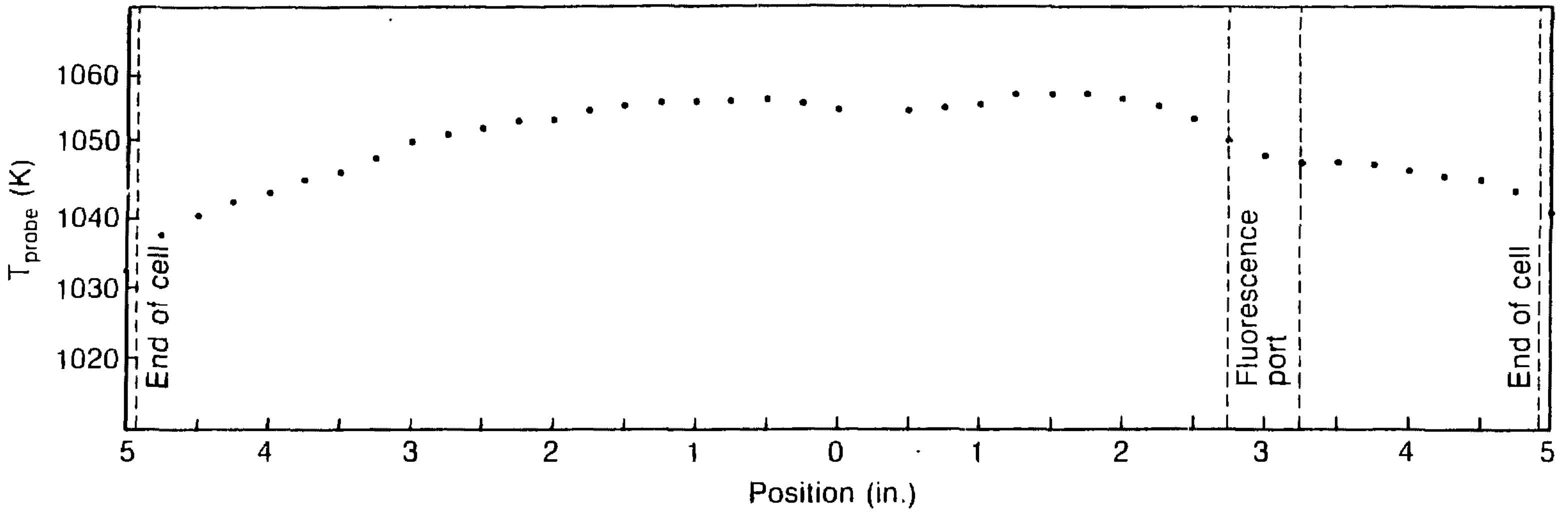

XBL 8511 11554

Fig. III-9. Temperature profile of the main oven.

From these data, the temperature correction factor is C=[1-0.063] with an estimated uncertainty of ±1%.

The temperature of the reservoir determines the thallium vapor density, but the temperature of the thallium reservoir is not accurately represented by the stem oven temperature as determined by the thermocouple, so we cannot rely on published values of the vapor pressure versus temperature to determine the density. However, precisely reproducing the stem oven temperature reproduces the same thallium vapor density for fixed main oven temperature. The reliability of the stem oven temperature is illustrated in Figure III-10, which shows the one-to-one correspondence of $\mu'\ell'$ (proportional to n) to the temperature of the stem oven. Assuming the actual temperature of the reservoir is proportional to the temperature of the stem oven, then applying the Clausius-Clapeyron equation, $P \alpha e^{-q/kT}$ (Landau 80), and the ideal gas law, P = nkT, (both applicable at low density) one expects $\ln(\mu'\ell' T_{stem}) \alpha -1/T_{stem}$. This relationship is verified by Figure III-11. Therefore, it is important to know precisely the stem oven temperature throughout an entire day of data collection so that the Stark measurement and the density calibration can be made at the same vapor density (i.e., stem oven temperature).

2. Electric Field Calibration

An electric field over one thousand volts per centimeter is needed to produce a significant absorption due to the Stark effect. It is also necessary to have the field change sign on a pulse to pulse basis in order to cancel instrumental asymmetries. In addition, the electric field pulses must be short to prevent discharges from occurring in the

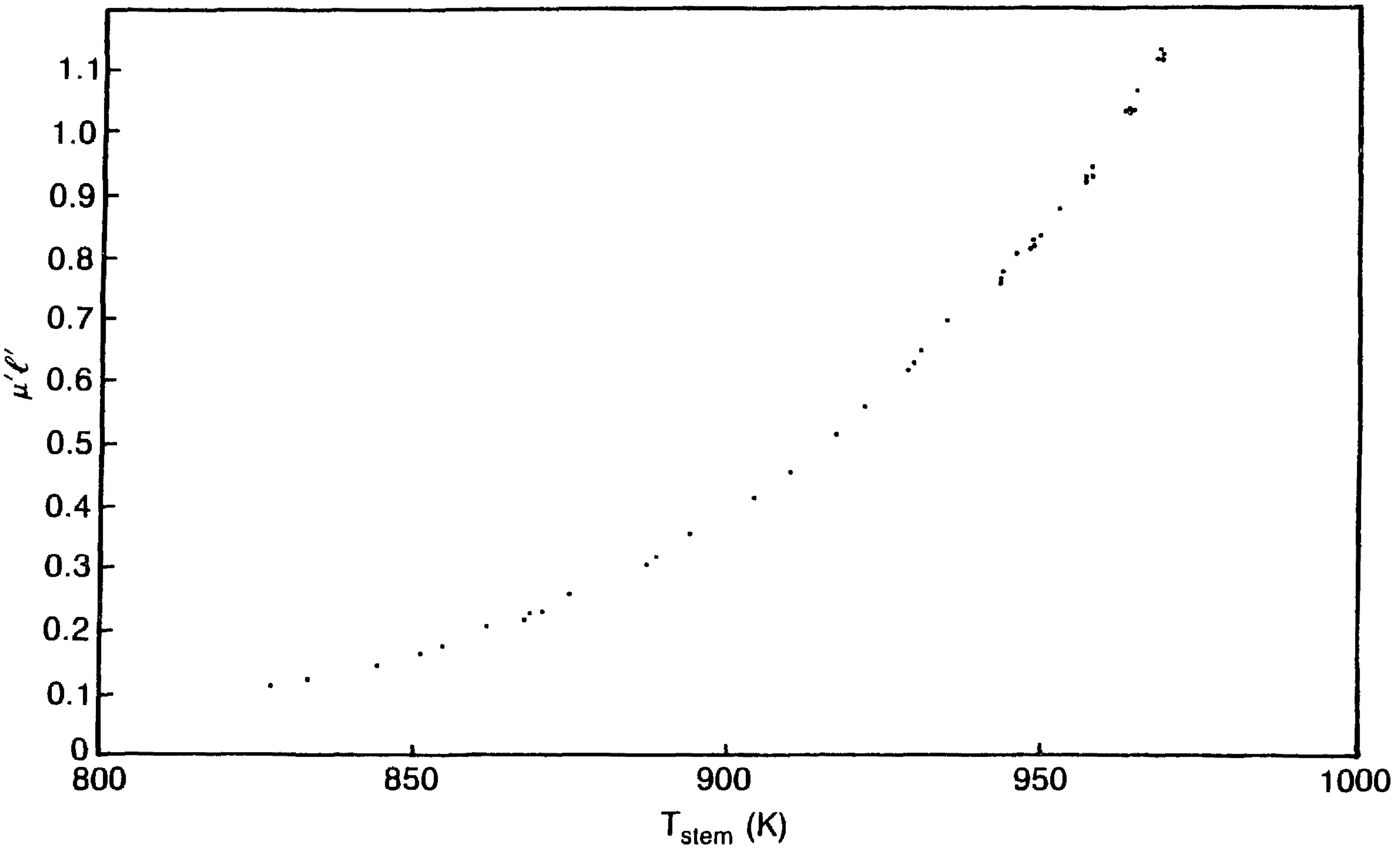

XBL 8511-11541

Fig. III-10. Density calibration ($\mu'\ell'$ proportional to n) plotted versus stem oven temperature (precision in each point ≈ 0.6%).

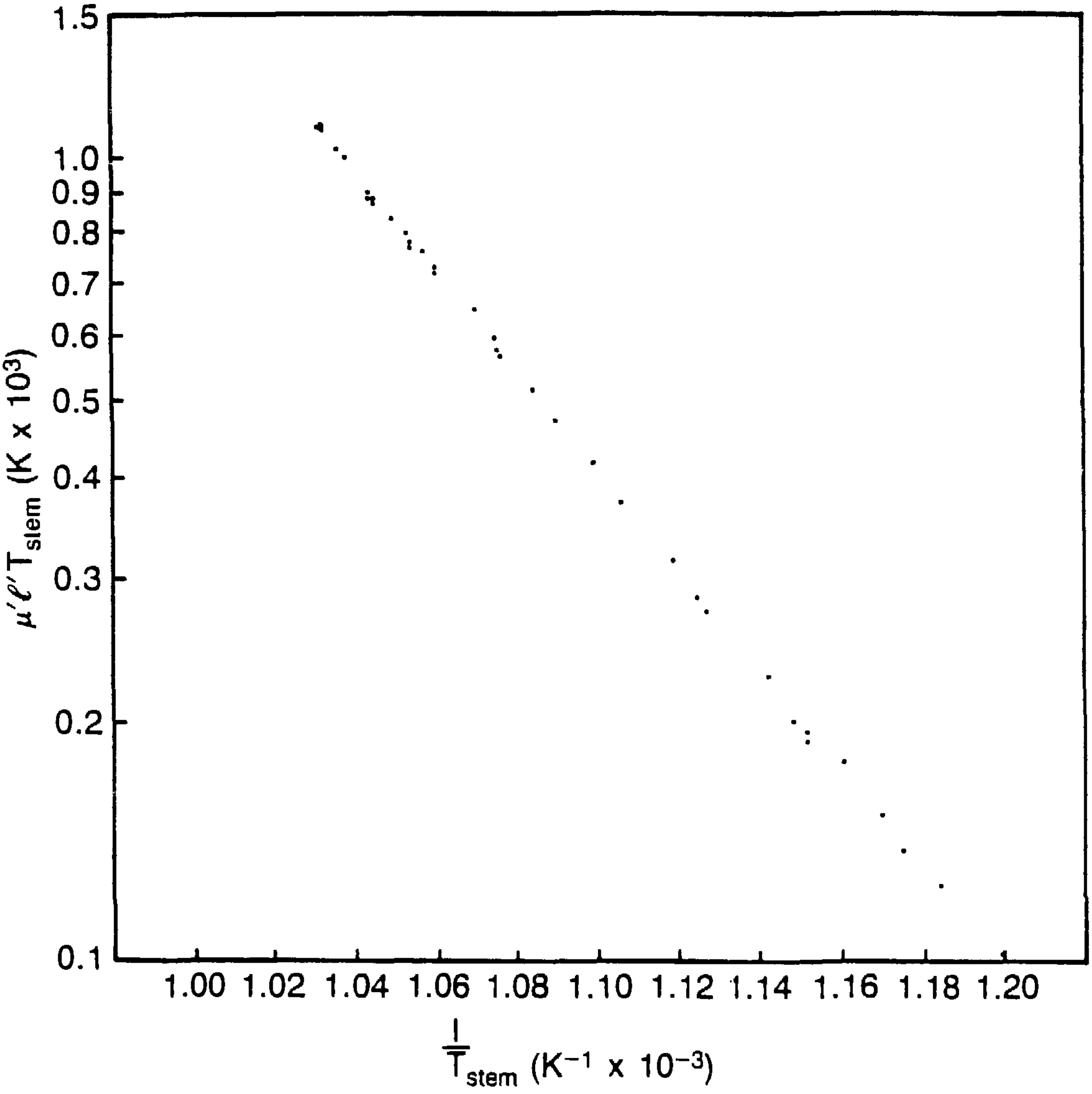

XBL 8511-11542

Fig. III-11. The Clausius-Clapeyron equation is illustrated by this plott of $\mu'\ell'$ T_{stem} versus $1/T_{stem}$.

cell at the densities used. For these reasons, a high voltage pulser with a fast rise and fall time was employed.

Details of the pulser design are described elsewhere (Drell 83), but its main features are described here. A regulated DC high voltage supply (Hewlett Packard 6516A) charges a coaxial delay line through a 10MΩ resistor. A stack of SCR's holds off the voltage until a signal synchronized with the laser pulse causes them to conduct, producing a voltage pulse with 15 nsec rise time, 20 nsec fall time and 100 nsec duration. The output passes through a mercury relay, which terminates the pulser with a 111Ω resistor to ground for electric field-off data or a 110Ω resistor in parallel with the cell electrodes for electric field-on data where the status of the relay is controlled by a computer signal. Thus, the pulser is fired on every laser shot so that no asymmetry arises between electric field off and electric field on, due to the influence of fast high voltage pulses on the detectors. Figure III-12 shows the electrical connections to the cell.

The electric field is calibrated by directly measuring the voltage on the plates for a given high voltage setting; then the electric field is determined by the electrode spacing. For measurements actually used to determine α, the field was 1700 V/cm ± 1%.

The geometry of the electrodes, cell, and ovens affects the electric field along the path of the laser beam. For measurements used to determine α and β, the total absorption is sensitive to $\int_0^{\ell'} E_z^2\, dx$ where E_z is the component of electric field $\perp$ to the electrodes, and the propagation direction of the laser beam is assumed to

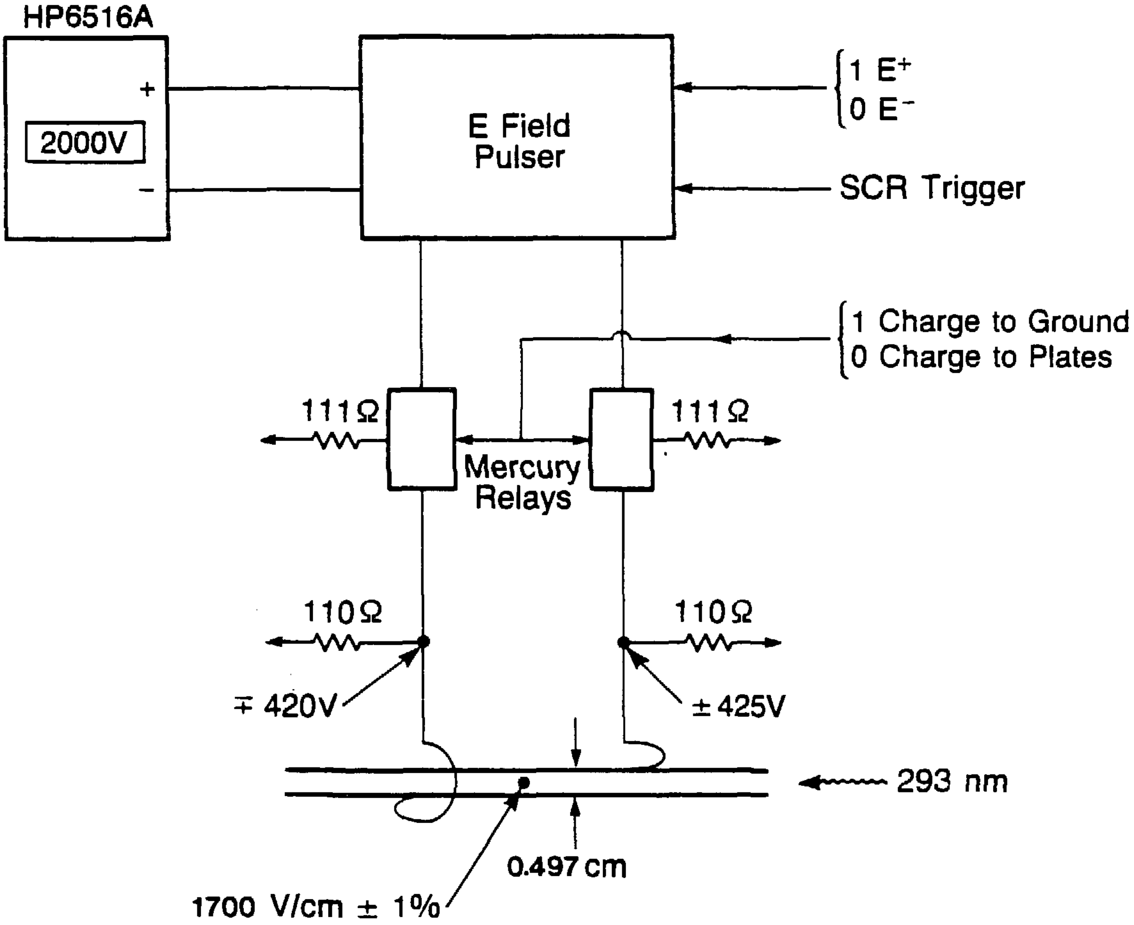

XBL 8511-11551

Fig. III-12. Electrical connections to electric field plates.

be along the center line between the electrodes. However, numerical solution of Laplace's equation by the relaxation method for the electrode-cell-oven geometry reveals that corrections for electrode end and width effects are less than 0.1% and negligible. Quantitatively,

$$\frac{\left(\int_0^{\ell'} E_z^2 \, dx\right)_{\substack{\text{RELAXATION}\\ \text{METHOD}}}}{\left(\frac{V\ell}{d}\right)^2} \simeq 1.0008$$

where V is the voltage between the plates, d is the separation, and ℓ is the length of the electrodes.

B. Lasers, Optics, and Detectors

1. Stark Absorption Measurement

The high intensity 292.7 nm light needed to drive the $6^2P_{1/2} \rightarrow 7^2P_{1/2}$ transition is generated by a dye laser oscillator-amplifier system with frequency doubling. The output of a frequency stabilized cw dye laser (Coherent Inc. Model 599-21) pumped by an argon ion laser (Coherent Inc. Model CR-6 retrofitted Inova) is amplified by a system of three amplifiers pumped by the doubled output of a Q-switched Nd:YAG laser (Quanta Ray DCR oscillator). Details of the system are described elsewhere (Drell 78). The laser delivers 585 nm photons in 8 nsec pulses at 17 Hz repetition rate in an 160 MHz band width with typical pulse energies of 10-15 mj/pulse. The beam is approximately 3 mm in diameter, and passes unfocused through an angle tuned KDP crystal (Cleveland Crystals 12 mm x 12 mm x 30 mm). UV light at 293 nm is generated with 30 efficiency. The UV beam is separated from the visible by a fused silica Brewster angle prism.

The UV beam is initially linearly polarized in the horizontal direction, and passes through a Pockels cell, which fixes the polarization relative to the electric field direction. The Pockels cell is a KD*P crystal 10 mm in diameter and 30 mm long (Cleveland Crystals QX 1020). Acting as a half-wave plate, the Pockels cell is used to switch the photon linear polarization between horizontal ($\hat{\varepsilon}\perp\vec{E}$) for measuring β, and vertical ($\hat{\varepsilon}\parallel\vec{E}$) for measuring α. The $\lambda/2$ voltage for the Pockels cell is 1548V delivered in a 1 msec pulse with a 100 μsec rise time.

The beam, collimated by two apertures 1 mm in diameter and 1 m apart, enters the vacuum tank through a Suprasil window (Amersil), passes through the cell, and exits through a second window. The windows of the vacuum tank are canted to prevent unwanted reflections from entering the cell. The beam is aligned manually with the two collimating apertures and a third alignment aperture behind the vacuum tank using two UV mirrors before the Pockels cell. All three apertures are initially aligned with the center line of the cell using a Helium-Neon laser.

The partially absorbed 293 nm beam is detected with an ITT FW114A photodiode. The anode of the tube is capacitively coupled to a charge integrating preamplifier mounted inside the detector housing. The preamp consists of an optimized RC integrator and a high speed unity gain buffer amplifier designed to source large currents. Figure III-14 shows the detector and preamp circuit. The preamp output is amplified and shaped by a high rate linear amplifier (LBL 11X5501). The peak voltage is sampled and held by a pulse stretcher (LBL 11X9421), then digitized by a 14 bit analog-to-digital converter

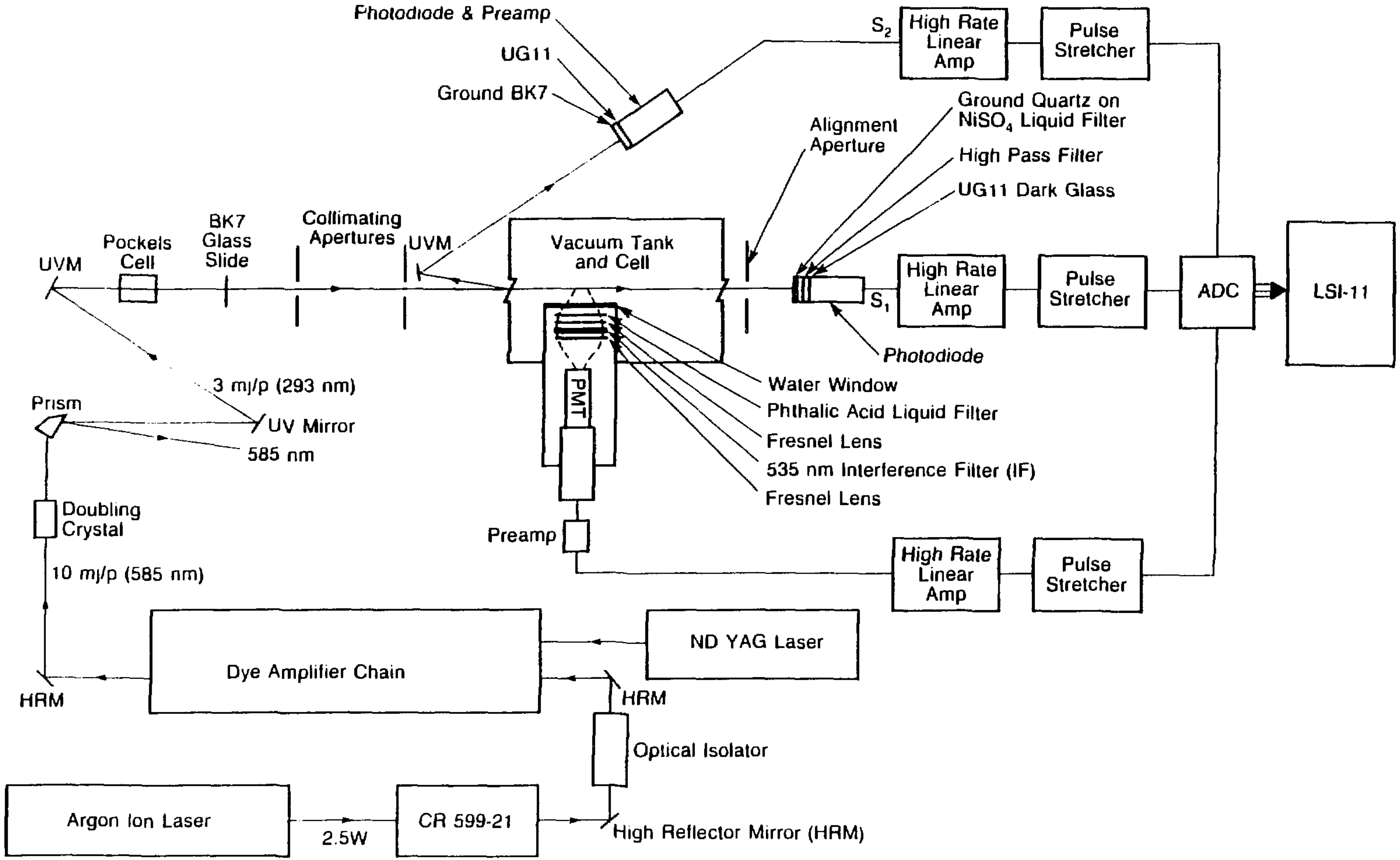

XBL 8511 11537

Fig. III-13. Schematic diagram showing the path of 293 nm laser beam for the Stark absorption measurement.

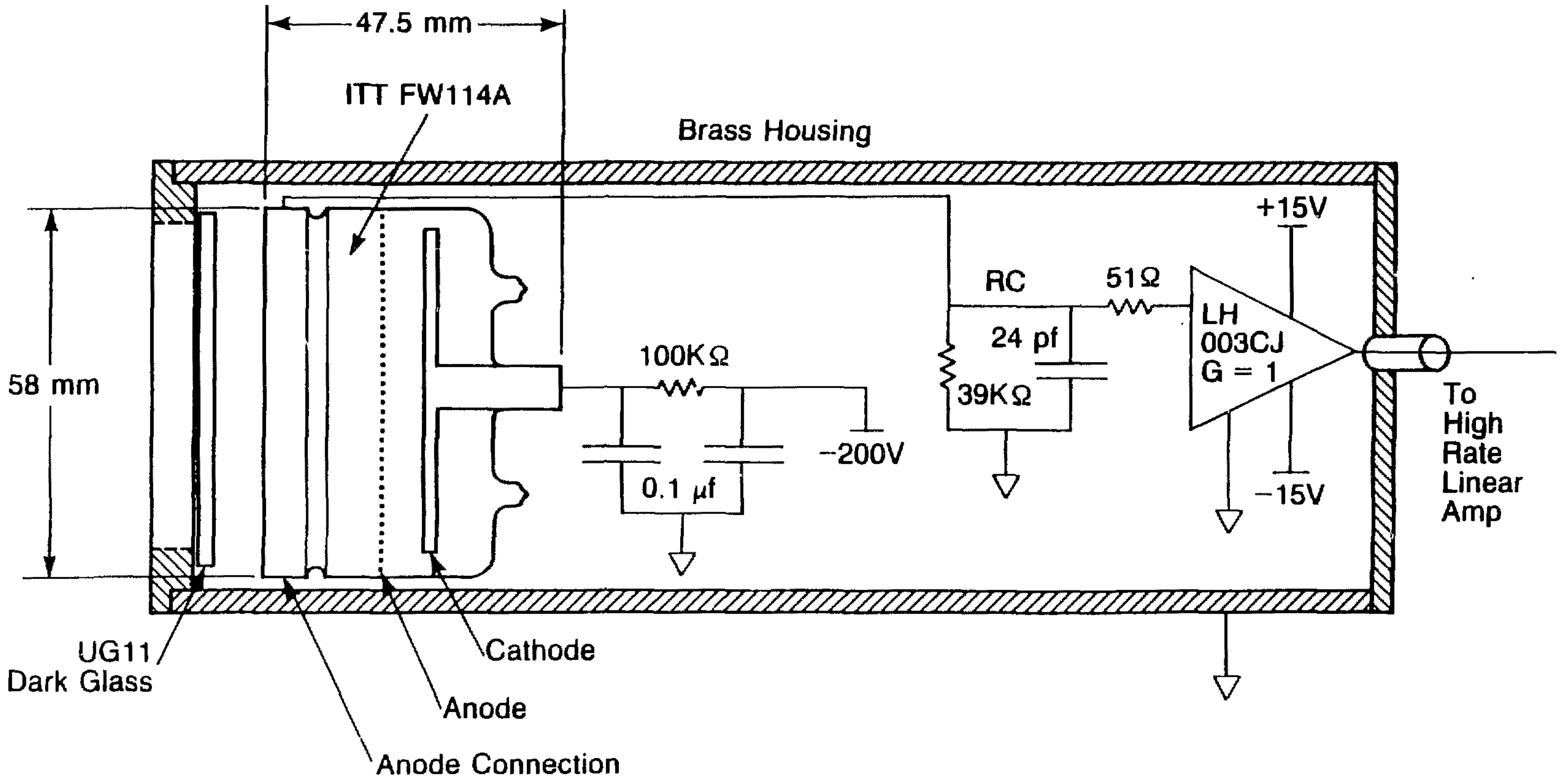

XBL 8511-11534

Fig. III-14. Schematic diagram of 293 nm detectors for the Stark absorption measurement.

(ADC), and stored in the computer. A reflected light beam from the vacuum tank entrance window is similarly detected to normalize the laser intensity.

The mode structure and alignment of the UV beam as well as cleanliness of the vacuum tank windows and the alignment of the detectors all affect the signal-to-noise ratio. All are optimized before measuring the Stark absorption.

The 535 nm light from the decay of the $7^2S_{1/2}$ state is also detected, and the magnitude of this signal is analyzed for its frequency dependence to locate the $6^2P_{1/2} \rightarrow 7^2P_{1/2}$ resonance. The fluorescence light passes through a port in the main oven and heat shields, and is detected with a photomultiplier tube. In front of the phototube is a series of Fresnel lenses and filters to collect the light. A phthalic acid liquid filter blocks scattered laser light (Kasha 48). The remaining light is collimated by a Fresnel lens, and passes through a 535 ± 2 nm interference filter followed by a second Fresnel lens, which focuses the fluorescence light on the phototube. The detector optics are enclosed in a water cooled brass housing to protect them from the heat, and recessed into the vacuum tank close to the oven. The anode of the phototube is connected to a preamp, linear amplifier, pulse stretcher, and ADC where it is read by the computer.

2. Density Calibration Absorption Measurements

The 535 nm light needed to drive the $6^2P_{1/2} \rightarrow 7^2S_{1/2}$ transition for calibrating the density is generated by a frequency stabilized cw dye laser (Coherent Inc. Model 599-21) pumped by an argon ion laser

(Cohrent Model CR-6 retrofitted Inova). Coumarin 540 (Exiton) dye is used at a concentration of 0.40 g/l in a solution of 40% benzyl alcohol and 60% ethylene glycol. In addition, 7 g of 9-methyl anthracene per liter of dye solution is used as a triplet state quencher which increases the dye laser output power and the dye life time.

The dye laser is pumped with 3.25 W of 488 nm argon laser light, and generates 25 mW of 535 nm light in a 2 mm diameter beam. Great care was taken to avoid stimulated emission effects by studying μ' versus I_0 over a range of several orders of magnitude and by finally keeping the 535 nm beam intensity very low. Figure III-15 shows the path of the beam, and the arrangement of neutral density filters chosen to attenuate the beam for this absorption measurement.

After passing through the vacuum tank and cell, the partially absorbed 535 nm beam is detected by an ITT FW114A photodiode. A similar photodiode is used to detect the beam reflected from the 5% neutral density filter in front of the vacuum tank to normalize the intensity. In order to prevent background light from entering the detectors, a 535 ± 2 nm interference filter is placed over each photodiode, and the measurements are made with the room lights off. The cw laser light produces a DC signal in the photodiodes. Each signal is amplified with a Princeton Applied Research (PAR) Model 113 preamplifier. The output of the amplifiers are digitized and stored in a computer, and are displayed on an oscilloscope for visually observing the absorption. Figure III-16 is a schematic diagram of the detectors.

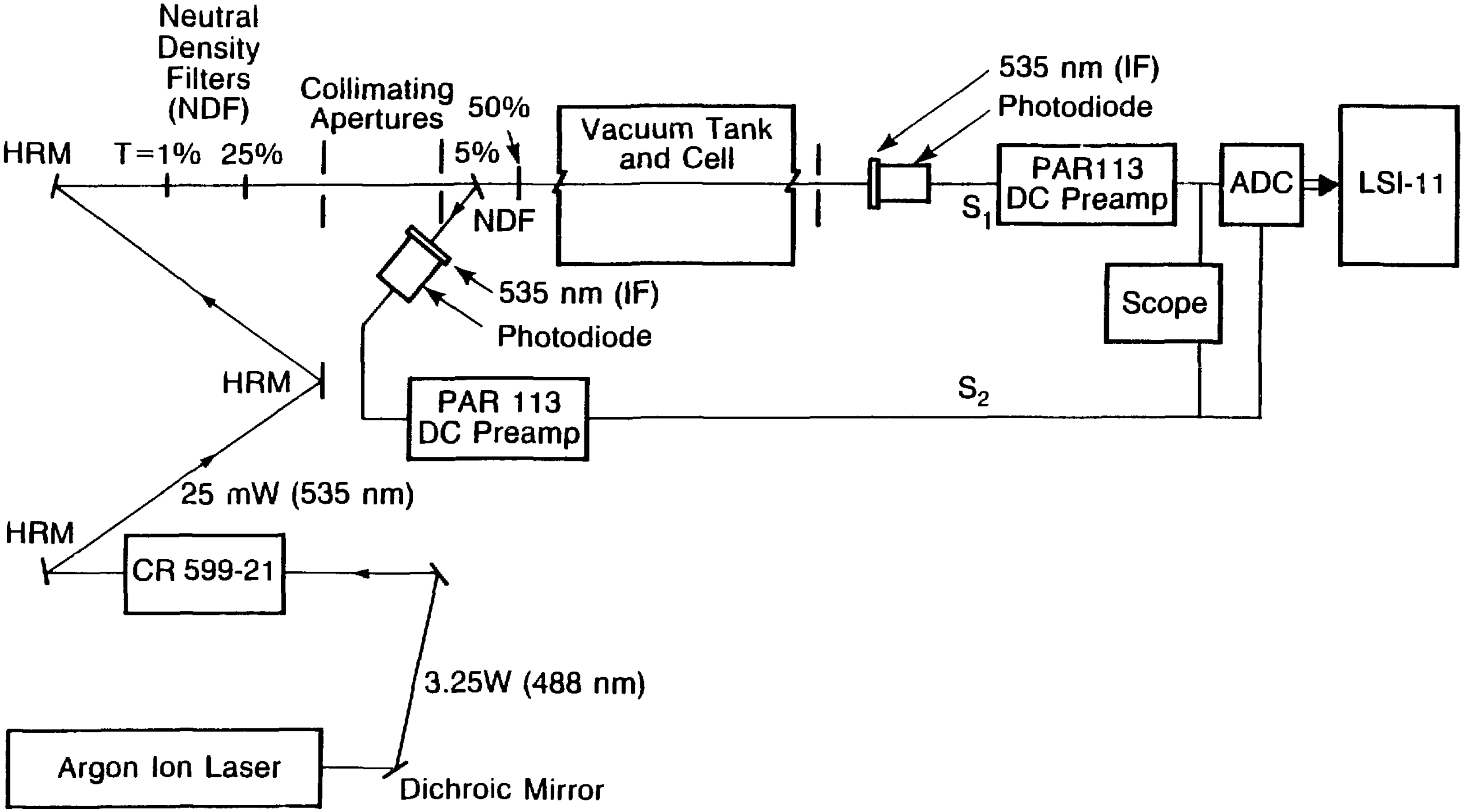

XBL 8511-11523

Fig. III-15. Schematic diagram showing the path of 535 nm laser beam for the density calibration.

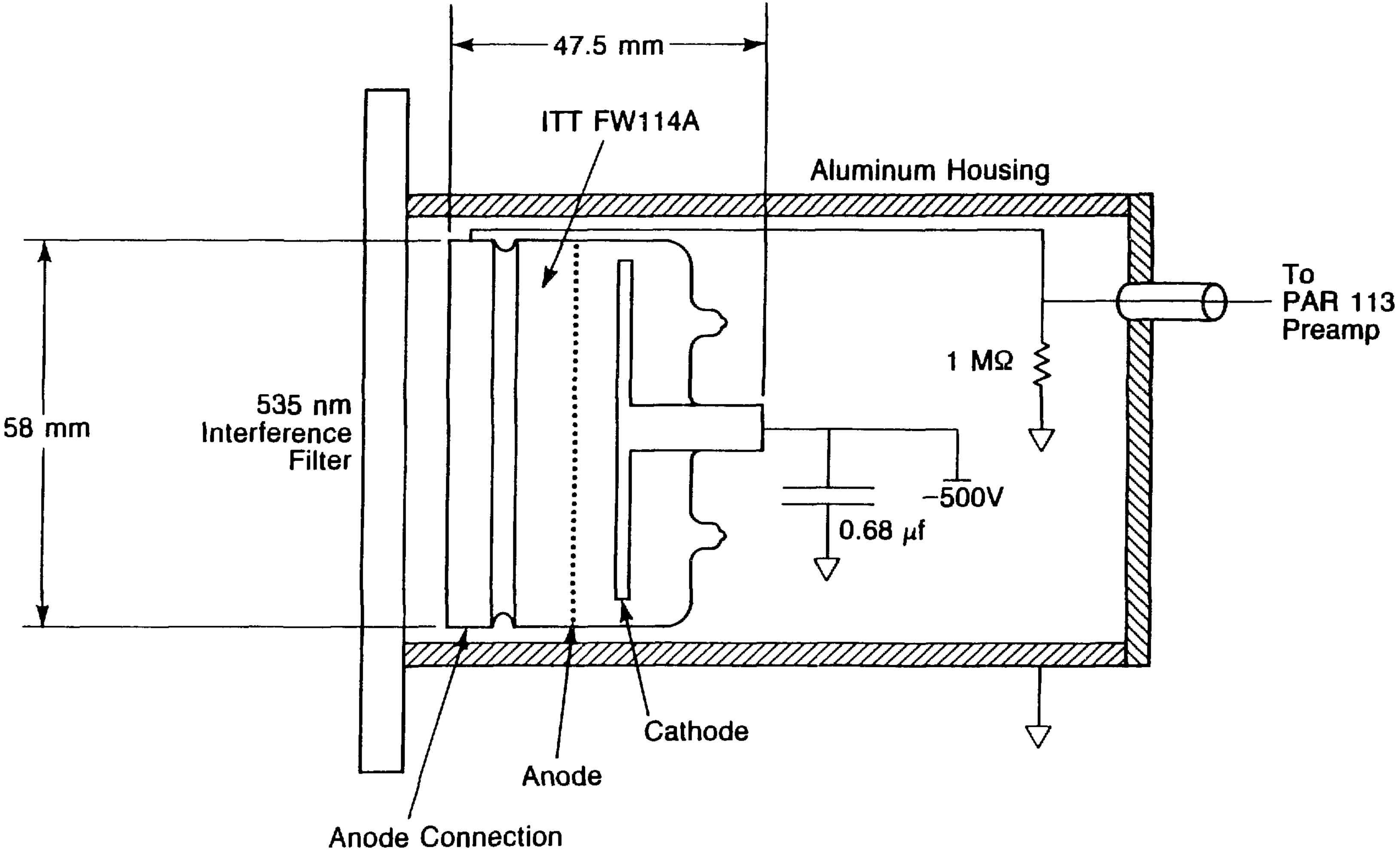

XBL 8511-11525

Fig. III-16. Schematic diagram of 535 nm detectors.

The 291.8 nm light needed to drive the $6^2P_{3/2} \rightarrow 7^2D_{5/2}$ transition in order to test the density calibration is generated by a frequency stabilized cw dye laser with frequency doubling. Rhodamine 590 dye (Exciton) is used at a concentration of 1 g per liter of ethylene glycol. The dye laser is pumped with 2.5 W on all lines of the argon ion laser, and produces 100 mW in a 2 mm diameter beam at 583.6 nm. The output of the dye laser is focused with a long focal length lens on the KDP doubling crystal, generating UV light at 291.8 nm collinear with the visible beam. The UV beam is aligned with the cell by steering the visible beam through two collimating apertures and the vacuum tank using two UV mirrors. Figure III-17 shows a schematic diagram of this absorption measurement.

After the beam passes through the vacuum tank and cell, the UV light is detected in a photomultiplier tube (RCA Model 8850). The 583.6 nm light is filtered by UG11 dark glass mounted on the front of the PMT housing. An additional reflection from a UV mirror before the detector removes background red light generated by the main oven which can pass through the UG11 filter. No normalization was used for this absorption measurement. The DC signal from the photomultiplier is amplified with a PAR Model 113 preamplifier, then digitized and stored in the computer.

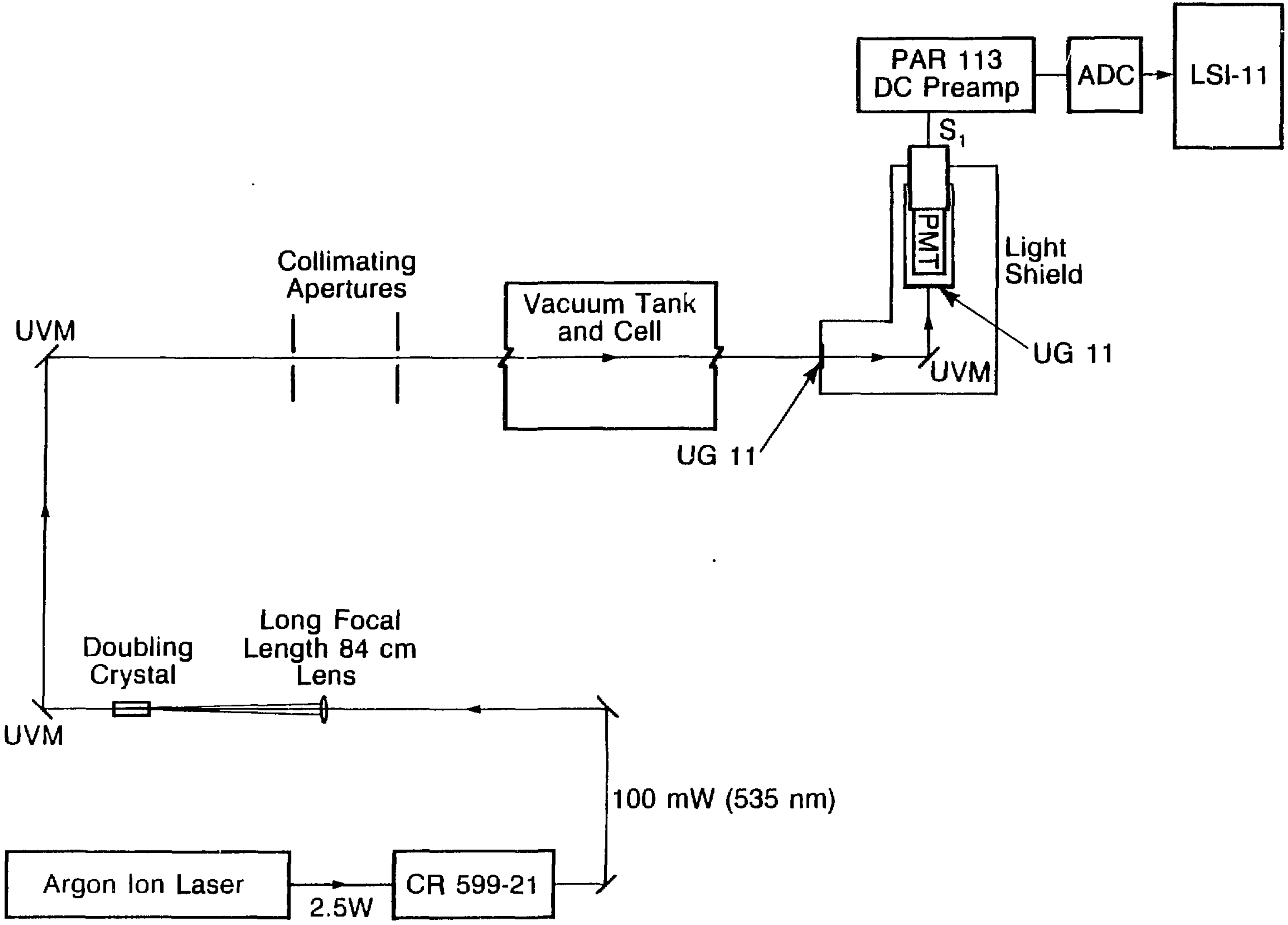

Fig. III-17. Schematic diagram showing the path of 291.8 nm laser beam.

XBL 8511-11524

IV. DATA ACQUISITION

A. Stark Measurements

When measuring the Stark absorption in the $6^2P_{1/2}F=1 \rightarrow 7^2P_{1/2}F=1$ transition, two signals are sent to the computer for each laser pulse. The first, S_1, is proportional to the 293 nm intensity after absorption, and the second, S_2, is proportional to the intensity before absorption. Computing the ratio, S_1/S_2, normalizes for pulse-to-pulse fluctuations in intensity. This ratio is binned by the computer according to the sign of $\vec{E}$ and the polarization direction, $\hat{\varepsilon}$, relative to $\vec{E}$.

$$
\begin{array}{ccc}
\text{SIGN OF E} & \hat{\varepsilon} & \text{TRANS. PROB.} \\
\begin{array}{c} + \\ - \end{array} & \left.\begin{array}{c} \parallel \\ \parallel \end{array}\right\} & 3\alpha^2E^2 \\
\begin{array}{c} + \\ - \end{array} & \left.\begin{array}{c} \perp \\ \perp \end{array}\right\} & 2\beta^2E^2
\end{array}
\qquad \text{(IV.1)}
$$

In a group of 16 laser pulses, four pulses of data are taken on each configuration in an order determined by a random number generator. In the next group of 16 laser pulses, four pulses of data are taken on each configuration with the electric field off. The ratio

$$
\frac{\left.\dfrac{S_1}{S_2}\right|_{E\text{ on}}}{\left.\dfrac{S_1}{S_2}\right|_{E\text{ off}}}
\qquad \text{(IV.2)}
$$

is then formed. The electric field-off data provides a means of normalizing for attenuation in the windows and mirrors, and differences in gain and efficiency of the detectors. This ratio is measured 64 times for each configuration. The measurements for E^+ and E^- are combined, and the average is computed, keeping separate the data for each polarization. This defines a preliminary data point for each polarization consisting of 1024 laser pulses.

In between each preliminary set of data, the 535 nm fluorescence of the $7^2S_{1/2}$ decay is observed, and the computer automatically centers the laser frequency on the peak of the resonance. The preliminary data sequence is then repeated four times, and the average comprises one data point for both α and β polarizations.

There is also an electric-field dependent background. In order to correct for this background, data are similarly taken 8 GHz off resonance, keeping separate the data for each polarization. Then the ratio

$$\left.\frac{\left.\dfrac{\left.\frac{S_1}{S_2}\right|_{E\text{ on}}}{\left.\frac{S_1}{S_2}\right|_{E\text{ off}}}\right|_{\text{on Res}}}{\left.\dfrac{\left.\frac{S_1}{S_2}\right|_{E\text{ on}}}{\left.\frac{S_1}{S_2}\right|_{E\text{ off}}}\right|_{\text{off Res}}}\right|_{\alpha,\beta} = e^{-\mu_{EXP}} \simeq 1 - \mu_{EXP} \tag{IV.3}$$

is constructed to provide a single experimental measurement of the absorption coefficient, μ_{EXP}. This quantity is measured repeatedly until the error in the mean is approximately ±4%. Usually, this requires 20 measurements of μ consisting of a total of 164,000 laser pulses, which requires 5 hrs of real running time. The sequencing of data collection is automatically controlled by the computer (LSI-11/2).

The largest absorption occurs on $6^2P_{1/2}F=1 \rightarrow 7^2P_{1/2}F'=1$ transition where the absorption coefficient, μ, is proportional to $3\alpha^2E^2$ for $\hat{\epsilon}\|\vec{E}$. To accumulate data with the best statistical precision, the majority of data is collected exclusively for $\hat{\epsilon}\|\vec{E}$. Figure IV-1 shows the linear dependence of the absorption coefficient on the square of the electric field strength. An experimental value for the coefficient α is obtained by collecting many hours of data at $E = 1700$ V/cm (2000 V setting on HV power supply). The coefficient β is determined by combining the measurement of α with a precise measurement of the ratio $\frac{\beta}{\alpha}$ obtained by observing the $7^2S_{1/2}$ decay fluorescence.

When measuring the ratio of β to α, the fluorescence is observed as a function of frequency by scanning the laser through the $F=0 \rightarrow F'=0$ and $F=0 \rightarrow F'=1$ transitions while switching the polarization between $\hat{\epsilon}\|\vec{E}$ and $\hat{\epsilon}\perp\vec{E}$. The ratio of the fluorescence signal to the normalization signal is computed to remove pulse-to-pulse fluctuations in intensity. This ratio is averaged over 64 pulses on each polarization for fixed frequency. The computer controls switching of the Pockels cell, and stepping of the laser frequency through the resonance. These data are shown in Figure IV-2 where a significant amount of fluorescence background is evident. To provide a quantitative way of dealing with the background, the majority of the data is collected by measuring the

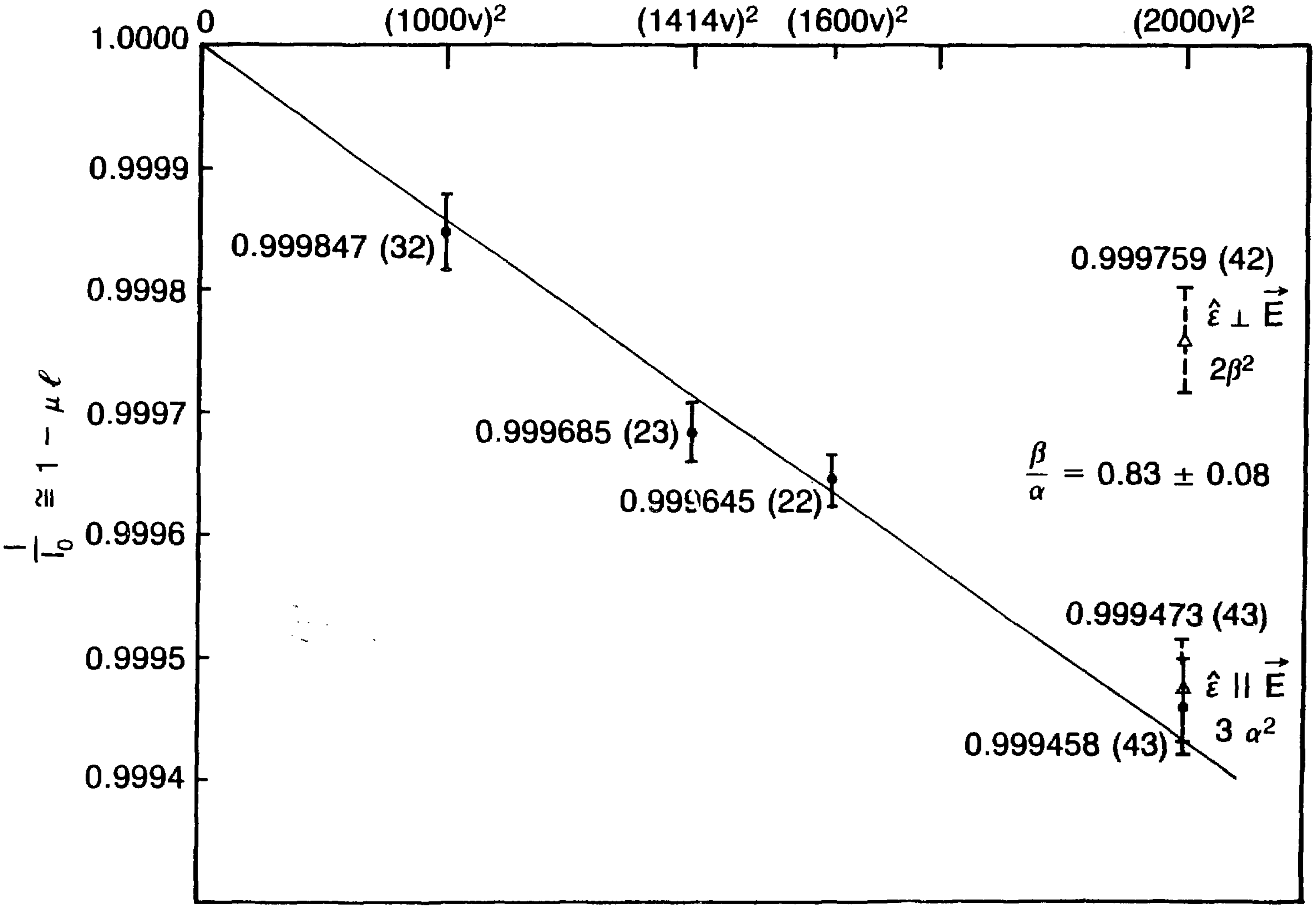

Fig. IV-1. Measurements of Stark absorption versus E^2 for $\hat{\varepsilon} \parallel \vec{E}$, $6^2P_{1/2}F=1 \rightarrow 7^2P_{1/2}F'=1$. Data are also shown for the measurements of β/α by absorption.

XBL 8511-11539

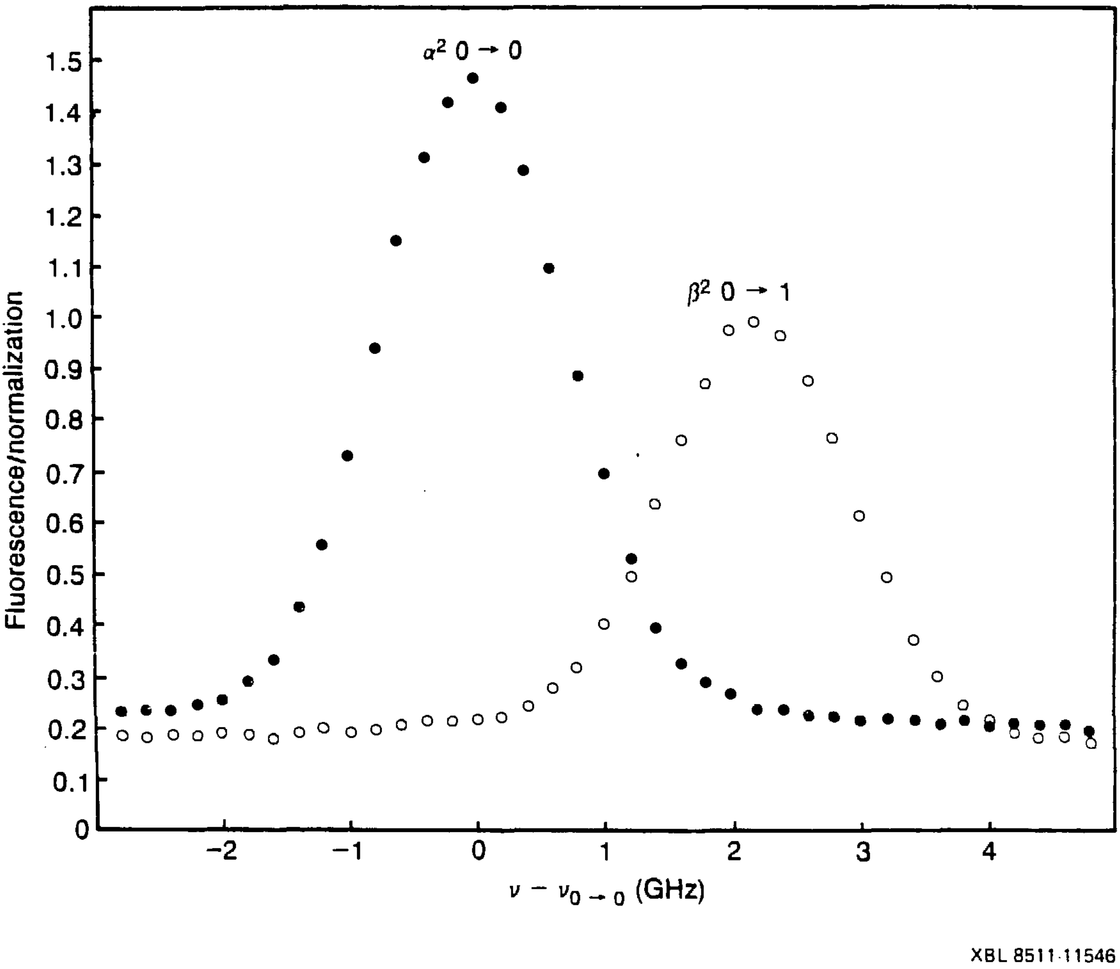

Fig. IV-2. Plot of $7^2S_{1/2}$ decay fluorescence versus frequency. The $6^2P_{1/2} \rightarrow 7^2P_{1/2}$:F=0 → F'=0, F=0 → F'=1 transition are driven while switching $\hat{\varepsilon} \parallel \vec{E}$, $\hat{\varepsilon} \perp \vec{E}$.

peak of the fluorescence versus the electric field for both hyperfine transitions. For the F=0 → F'=0 transition, the fluorescence signal is proportional to α^2E^2, and the peak fluorescence is measured at four values of E. Averaging over 640 laser pulses for each value of E, a statistical precision of ±0.4% is obtained for each measurement. The fluorescence signal for the F=0 → F'=1 transition is proportional to β^2E^2, and is similarly measured versus the electric field. The data plotted versus E^2 is shown in Figure V-1.

B. Density Calibration Measurements

The density calibrating experiments are run in a cw mode, so the data are collected in a slightly different manner. When measuring absorption in the $6^2P_{3/2} \to 7^2S_{1/2}$ (535 nm) transition, both an absorption signal, S_1, and a normalization signal, S_2, are sent to a 14 bit A to D converter. The two signals are read rapidly in succession. First, S_1 is converted and read by the computer, then ~3μsec later, S_2 is converted and read. The time between reading the absorption and normalization signals is short compared to the time scale for variation in the laser intensity. The signals are sampled approximately 100 times per second. The absorption is measured as a function of frequency. After 128 samples at a fixed frequency, the ratio S_1/S_2 is calculated to normalize for fluctuations in laser intensity. The computer remotely steps the laser frequency, and eventually scans the entire resonance. Figure IV-3 shows the $6^2P_{3/2} \to 7^2S_{1/2}$ absorption versus frequency. The Doppler width of the F=1 → F'=1 transition overlaps that of the F=2 → F'=1 transition, so the majority of data is

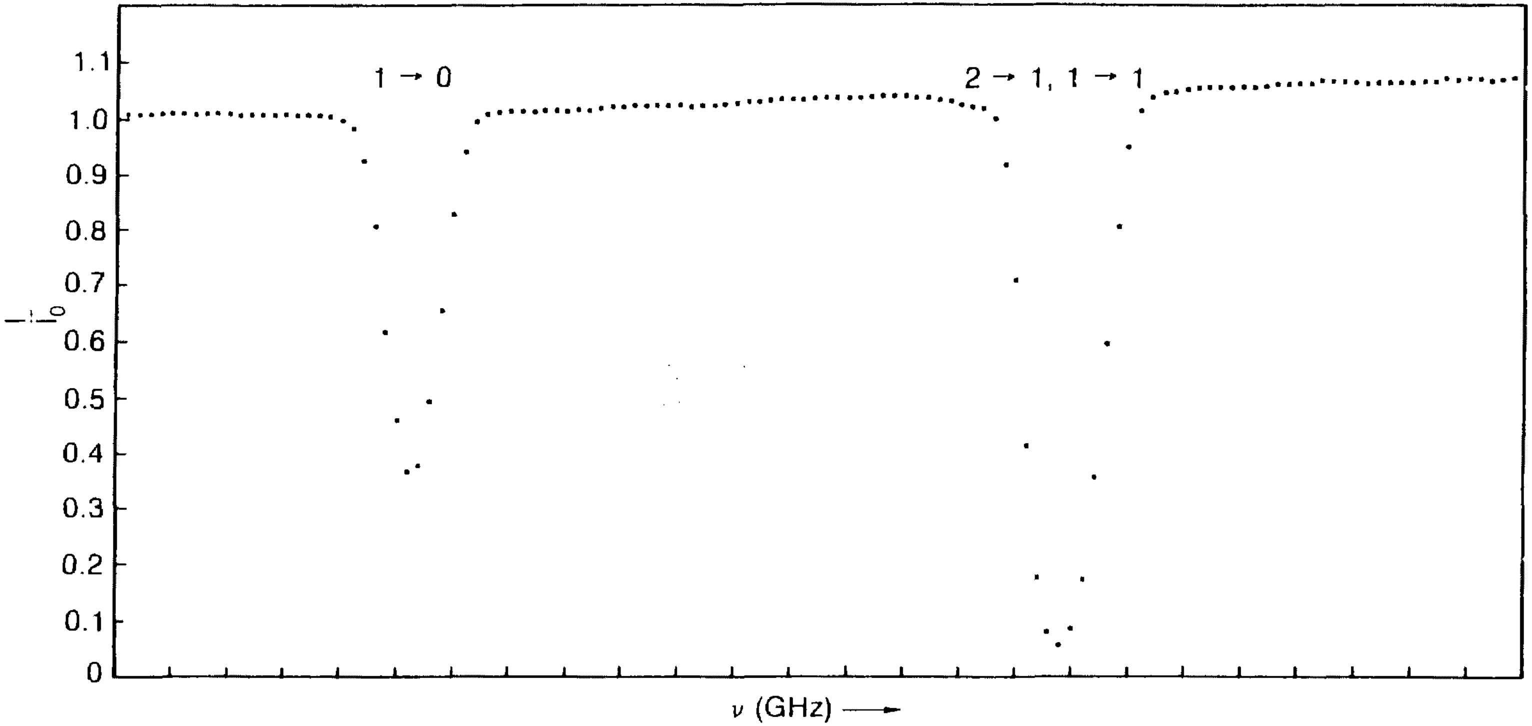

XBL 8511 11543

Fig. IV-3. Normalized intensity I/Io versus frequency for $6^2P_{3/2} \rightarrow 7^2S_{1/2}$.

collected on the F =1 → F'=0 transition. To correct for attenuation in the windows and mirrors, and differences in gain and efficiency of the detectors, the ratio

$$\frac{\left.\frac{S_1}{S_2}\right|_{\nu}}{\left.\frac{S_1}{S_2}\right|_{\substack{\text{off}\\ \text{Res}}}} = e^{-\mu'_{535}(\nu)\ell'} \tag{IV.4}$$

is calculated. Figure IV-4 shows the quantity $\mu'\ell'$ plotted versus frequency for a typical scan of the F=1 → F'=0 transition. The solid line is a Gaussian (Equation II.11) corresponding to Doppler broadening for the same temperature at which the data was taken. The agreement between the data and the expected line shape indicate that Lorentz broadening due to collisions and finite lifetime of the upper state is negligible. On a typical day of data collection, an average of 10 scans such as this is used to determine the absorption coefficient, resulting in a precision of ±0.2%.

In order to test this method of density calibration, the absorption coefficient in the $6^2P_{3/2} \rightarrow 7^2D_{5/2}$ (291.8 nm) transition is also measured in a similar way by scanning a weak cw monochromatic laser beam through the resonance. In this case, the normalization signal is not easily measured because of its low intensity. However, the laser intensity is actually quite stable, so it is assumed constant. Since the absorption signal is also small there is a background coming from detector and electronics noise, but this is easily measured by taking data with the laser beam blocked. The quantity

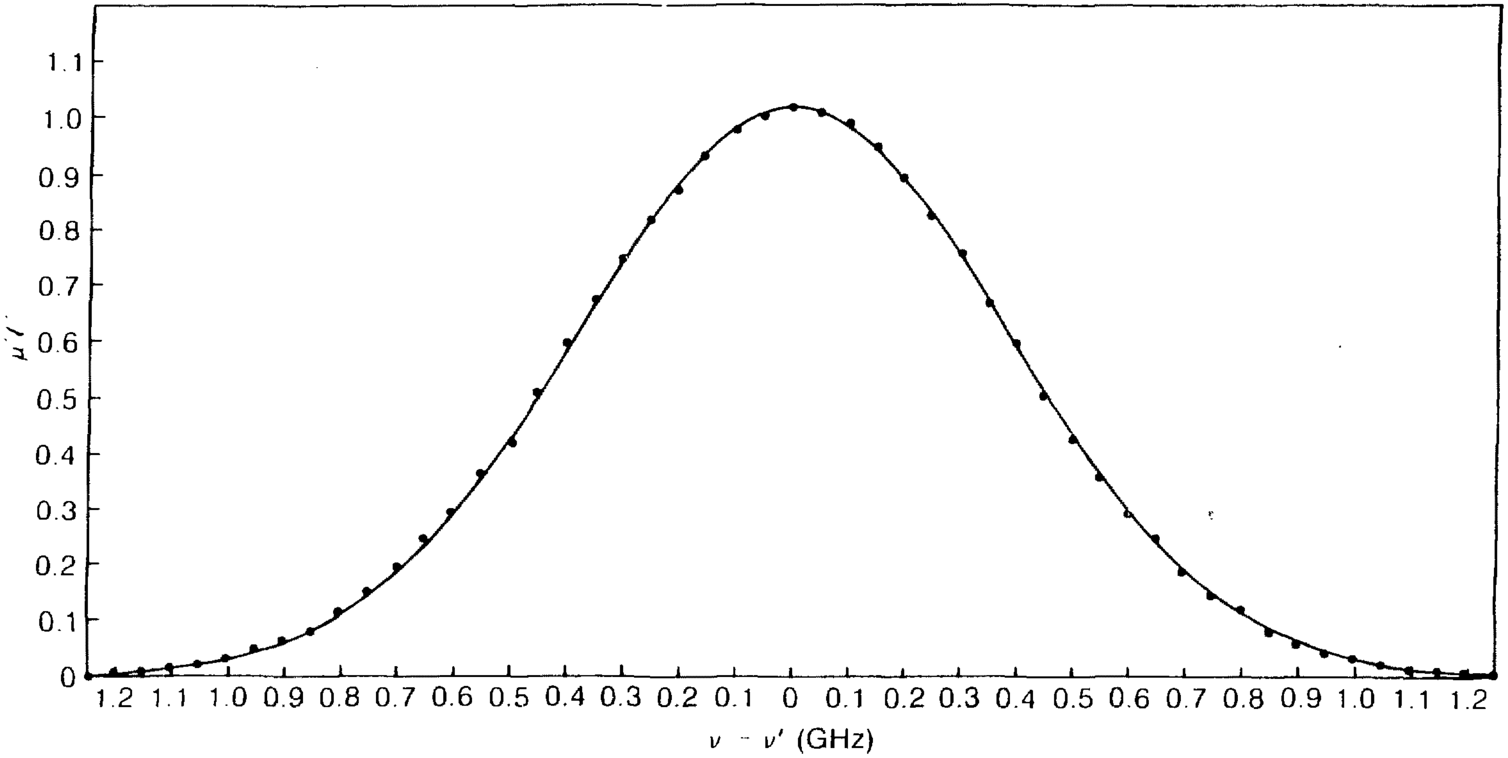

XBL 8511 11538

Fig. IV-4. Absorption curve for the transition $6^2P_{3/2}F=1 \rightarrow 7^2S_{1/2}F=0$ (535 nm). The quantity $\mu'\ell'$ is plotted versus frequency. Points: experimental data taken at effective vapor temperature T=1030K (precision in each point ≈ 0.6%). Solid curve $\mu'\ell'$ calculated from Equation II.2 for T=1030K and normalized to agree with experiment at $\nu=\nu'$.

$$\frac{S_1 - \text{Background}\Big|_{\substack{\text{on}\\ \text{Res}}}}{S_1 - \text{Background}\Big|_{\substack{\text{off}\\ \text{Res}}}} = e^{-\mu''_{291.8}(\nu)\,\ell'} \tag{IV.5}$$

determines the absorption coefficient for this transition. Figure IV-5 shows $\mu''\ell'$ plotted versus frequency where the data from 8 scans were combined. The expected line shape is the sum of two Gaussians because the hyperfine structure of the $7^2D_{5/2}$ state is not resolved, and the hyperfine structure of the $6^2P_{3/2}$ state is only partially resolved (see Equation II.14). Taking this into account, there is agreement between the data and the expected line shape shown in Figure IV-5 where only Doppler broadening is assumed. The signal to noise ratio in this measurement is lower than the previous measurement due to the low intensity of the 291.8 nm light. An average of 8 measurements is needed to determine the absorption coefficient to a precision of ±4%.

The ratio of the measured absorption coefficients in these two transitions determines the ratio of the coefficients for spontaneous emission according to the following formula:

$$\frac{A(7^2D_{5/2} \rightarrow 6^2P_{3/2})}{A(7^2S_{1/2} \rightarrow 6^2P_{3/2})} = \frac{\mu''_{291.8}\,\ell'}{\mu'_{535}\,\ell'}\;\frac{e^{\frac{-11220}{T_{main}} \big/ 535}}{e^{\frac{-11220}{T_{main}} \big/ 291.8}}\;\frac{1}{12}\;\frac{1}{(0.936)}\left(\frac{535\ \text{nm}}{291.8\ \text{nm}}\right)^3 . \tag{IV.6}$$

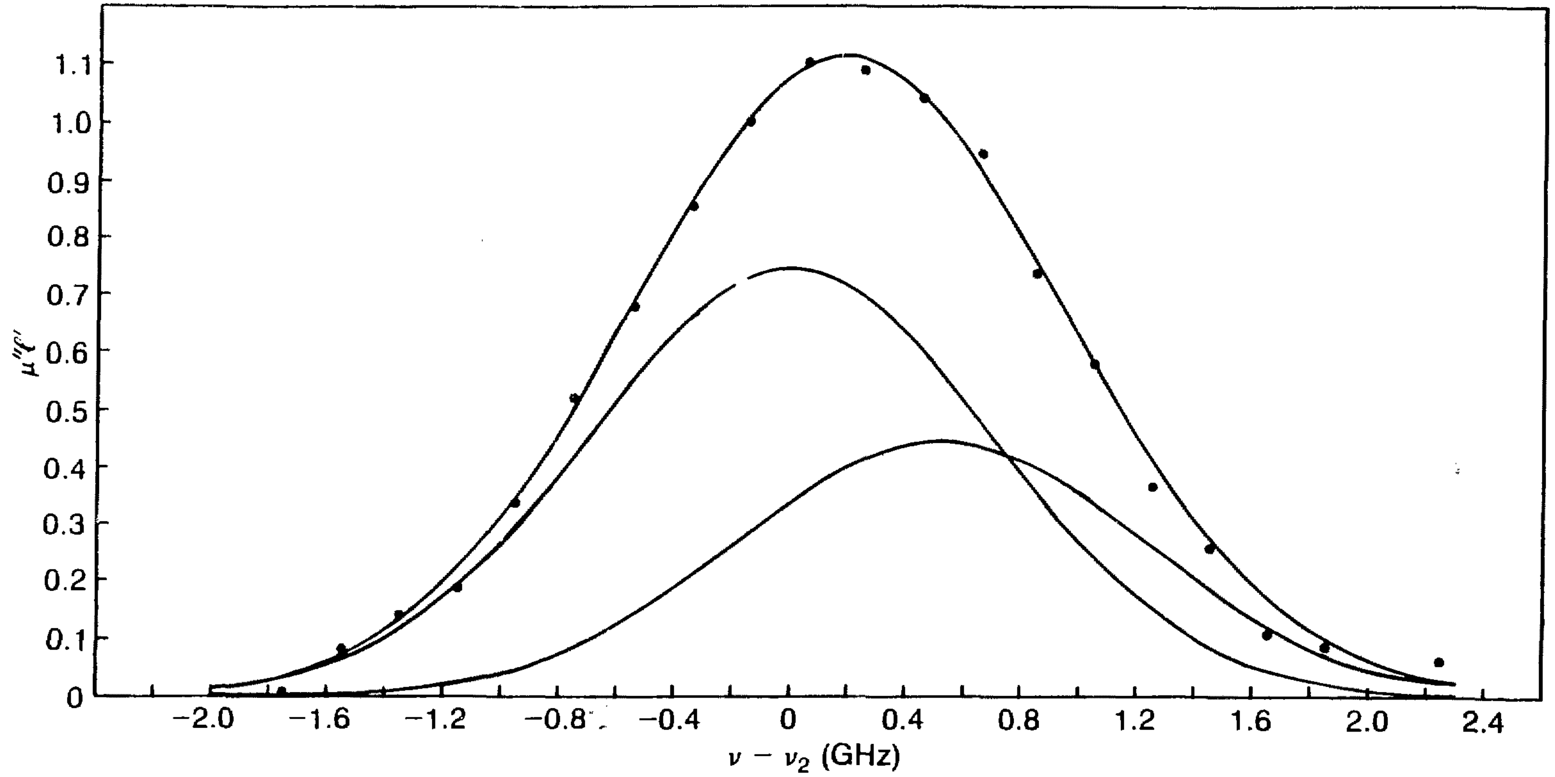

XBL 8511-11535

Fig. IV-5. Absorption curve for the transition $6^2P_{3/2} \rightarrow 7^2D_{5/2}$ (291.8 nm). The quantity $\mu''\ell'$ is plotted versus frequency. Points; experimental data taken at effective vapor temperature T=1032K (precision in each point ≈ 4%). Solid curve: $\mu''\ell'$ calculated from Equation II.15 for T=1032K and normalized to agree with experiment at $\nu=\nu_{peak}$.

This expression is independent of density because the absorption coefficients are measured at the same stem oven temperature. The experimental values are given in the following tabulation:

λ	$\mu\ell'$	T_{main}	T_{stem}	
291.8 nm	1.11 ± 0.042	1032 K	959.0 K	(IV.7)
535 nm	0.9393 ± 0.0080	1029 K	959.2 K	

The results of these measurements are

$$\frac{A(7^2D_{5/2} \rightarrow 6^2P_{3/2})}{A(7^2S_{1/2} \rightarrow 6^2P_{3/2})} = 0.635 \pm 0.025 \qquad \text{(IV.8)}$$

where the statistical uncertainty in the measurements are combined in quadrature with the estimated fractional uncertainty in the correction factor

$$\frac{\delta\{0.936\}}{\{0.936\}} \simeq 1\% \qquad \text{(IV.9)}$$

accounting for partial resolution of the hyperfine structure components. Combining the ratio with the precisely determined coefficient for spontaneous emission (Hsieh 72)

$$A(7^2S_{1/2} \rightarrow 6^2P_{3/2}) = (7.11 \pm 0.16) \times 10^7 \text{ sec}^{-1} \quad , \qquad \text{(IV.10)}$$

the coefficient

$$A(7^2D_{5/2} \rightarrow 6^2P_{3/2}) = (4.51 \pm 0.21) \times 10^7 \text{ sec}^{-1} \qquad \text{(IV.11)}$$

is obtained, and is in agreement with a previous determination (Gallagher 64)

$$A(7^2D_{5/2} \rightarrow 6^2P_{3/2}) = (4.2 \pm 0.5) \times 10^7 \text{ sec}^{-1} \quad . \tag{IV.12}$$

Although measuring the absorption coefficient in the $6^2P_{3/2} \rightarrow 7^2D_{5/2}$ transition is used to check the density calibration, only the absorption coefficient in the $6^2P_{3/2} \rightarrow 7^2S_{1/2}$ transition is actually employed in the determination of α.

V. RESULTS AND CONCLUSIONS

The Stark coefficient α is finally determined by measurements of the absorption coefficient in the $6^2P_{1/2}F=1 \rightarrow 7^2P_{1/2}F'=1$ transition where data were accumulated for several hours on three different days. Careful records of the temperatures were kept, and the density was calibrated by measuring the absorption coefficient in the $6^2P_{3/2}F=1 \rightarrow 7^2S_{1/2}F=0$ transition at the same average temperatures, usually on the same day. The tabulation in Figure V-1 summarizes the data.

α can be determined independent of the density from the ratio of the absorption coefficients by the following formula:

$$\alpha^2 = \frac{1}{3E^2}\,\frac{\mu\ell}{\mu'\ell'}\,e^{\frac{-11220}{T_{main}}}\,[1 - 0.063]\,\frac{A(7^2S_{1/2} \rightarrow 6^2P_{3/2})\lambda'^3}{32\pi^3}\,\frac{\ell'}{\ell} \tag{V.1}$$

where $\lambda' = 535$ nm, $\ell' = 25$ cm, $\ell = 23$ cm, and $A(7^2S_{1/2} \rightarrow 6^2P_{3/2}) = (7.11 \pm 0.16) \times 10^7\ \mathrm{sec}^{-1}$. For these measurements, $E = 1700$ V/cm. From the three sets of data, the three determinations of α (shown in the table) are all in agreement where the uncertainties:

$$\frac{\Delta E}{E} = 1\%$$

$$\frac{\Delta\ell}{\ell} = 1\%$$

$$\frac{\Delta\ell'}{\ell'} = 1\%$$

STARK ABSORPTION				DENSITY CALIBRATION				
$1-\mu\ell$	T_{main} (K)	T_{stem} (K)	NO. OF MEASUREMENTS	$\mu'\ell'$	T_{main} (K)	T_{stem} (K)	NO. OF MEASUREMENTS	α (10^{-5} cm/V)
0.999414(24)	1030	963.7	36	1.0215 ± 0.0012	1030	963.4	10	1.31 ± 0.03
0.999390(63)	1031	963.0	20	1.0250 ± 0.0007	1030	963.0	10	1.34 ± 0.07
0.999420(32)	1033	964.9	16	1.0900 ± 0.0023	1033	964.4	12	1.29 ± 0.04

Fig. V-1

$\frac{\Delta[1 - 0.063]}{[1 - 0.063]} = 1\%$ (uncertainty in the correction for the nonuniformity in T_{main})

$\frac{\Delta A}{A} = 2.25\%$

are combined in quadrature with the statistical uncertainties in $\mu\ell$ and $\mu'\ell'$. The weighted average of these three determinations of α yield a total fractional uncertainty of 2%. However, α is quoted with the uncertainty enlarged to 5% with 95% confidence.

$$\begin{aligned} \alpha &= (1.31 \pm 0.06) \times 10^{-5}\ \mu_0\ \mathrm{cm/V} \\ &= (247 \pm 12)\ a_0^3 \end{aligned} \qquad \text{(V.2)}$$

Next from the F=0 → F'=0 ($\hat{\varepsilon} \parallel \vec{E}$) and F=0 → F'=1 ($\hat{\varepsilon} \perp \vec{E}$) fluorescence signals shown versus E^2 in Figure V-2, the ratio of the slopes (determined by a least squares fit to a straight line) yields the result:

$$\frac{\beta}{\alpha} = 0.83 \pm 0.01 \quad \text{(95\% confidence)} \qquad \text{(V.3)}$$

which agrees with an earlier measurement (Chu 77),

$$\frac{\beta}{\alpha} = 0.84 \pm 0.05 \quad .$$

The ratio of β to α was also measured directly by absorption in the F=1 → F'=1 transition while switching the polarization, and the result

$$\frac{\beta}{\alpha} = 0.83 \pm 0.08$$

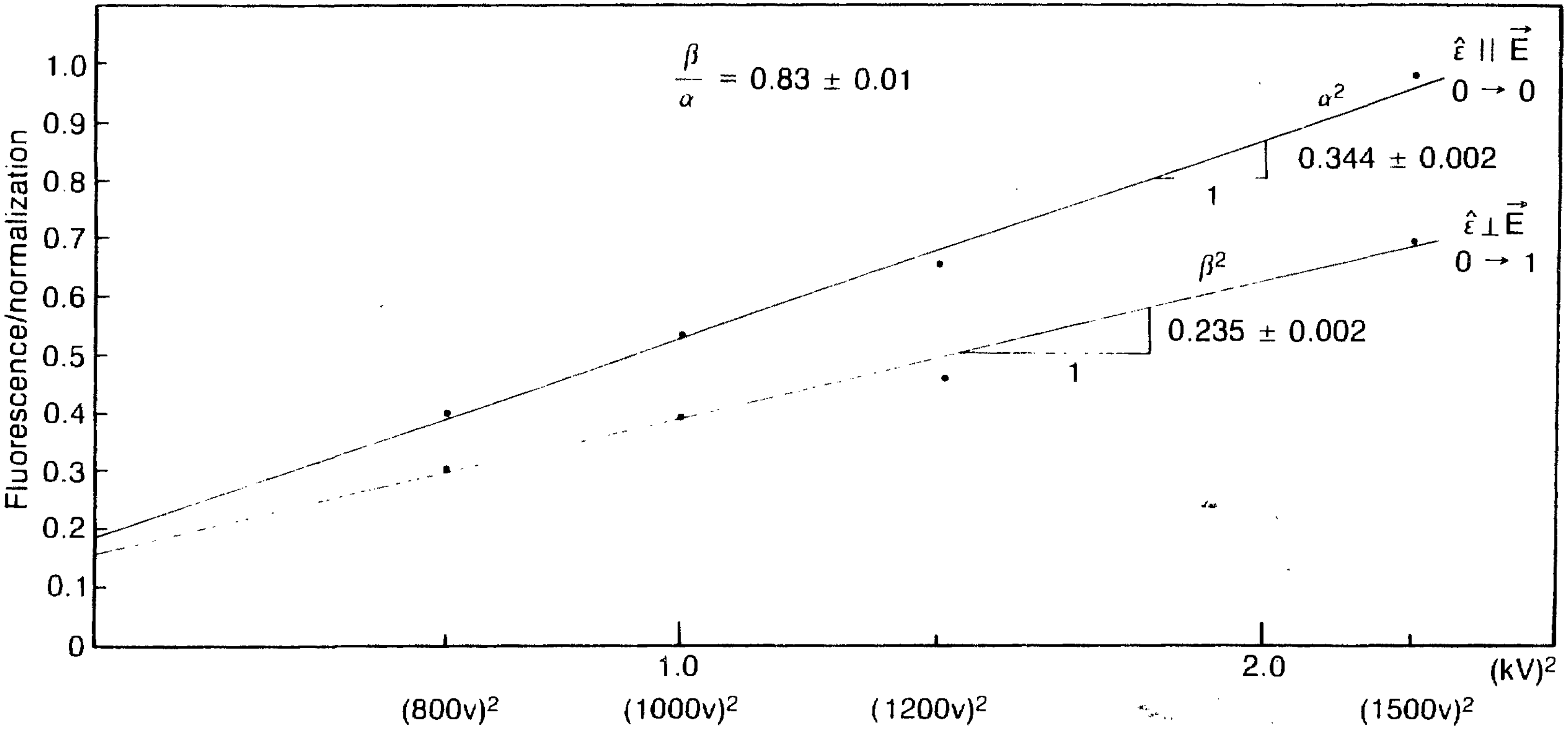

XBL 8511 11540

Fig. V-2. Intensity of $7^2S_{1/2}$ decay fluorescence versus E^2 (precision in each point ≈ 0.4%).

was obtained in agreement with the fluorescence measurement. Combining (V.2) and (V.3) determines

$$\begin{aligned}\beta &= (1.09 \pm 0.05) \times 10^{-5}\ \mu_0\ \text{cm/V} \\ &= (198 \pm 10)\ a_0^3 \quad .\end{aligned} \tag{V.4}$$

This may be compared with the naive theoretical estimate (Neuffer 77, Johnson 85):

$$\begin{aligned}\beta_0 &= 1.64 \times 10^{-5}\ \mu_0\ \text{cm/V} \\ &= 309\ a_0^3 \quad .\end{aligned} \tag{V.5}$$

The substantial discrepancy between (V.4) and (V.5) indicates that the valence electron is shielded from the external electric field to an appreciable extent by the core electrons.

From $\frac{\text{Im}\,\mathcal{E}_p}{\beta} = -(1.73 \pm 0.33)$ mV/cm (Drell 84,85), a value for the parity non-conserving E1 amplitude is obtained:

$$\begin{aligned}\text{Im}\,\mathcal{E}_p &= (-1.89 \pm 0.36) \times 10^{-8} \\ &= (1.67 \pm 0.32) \times 10^{-10}\ Q_W\end{aligned} \tag{V.6}$$

where $Q_W = Z(1-4\sin^2\theta_W)-N = -112.7$ is the weak charge for ^{205}Tl in the standard SU(2) x U(1) electroweak model. Here, θ_W is the Weinberg angle and $\sin^2\theta_W = 0.215$, while $Z = 81$ and $N = 124$ are proton and neutron numbers, respectively. Now, (V.6) can be compared directly with various estimates of $\mathcal{E}_p$ given in Johnson (85). However, because of the large discrepancy between (V.4) and (V.5), it is evident that substantial theoretical work remains to be done on many-body effects in the 293 nm transition amplitude. Considerable efforts are currently being directed at this problem (Johnson, Martensson, Das 85).

APPENDIX

Revised Value of M

The magnetic dipole amplitude (M) was originally measured (Chu 77) through interference with the Stark induced E1 amplitude αE:

$$\frac{M}{\alpha} = -\ 1.03 \pm 0.10 \text{ V/cm} \quad .$$

The published value of M was calculated from the naive theoretical estimate of the coefficient α_0 (II.8). Now that α is known experimentally, the value of M may be revised:

$$M = -(1.35 \pm 0.13) \times 10^{-5}\ \mu_0 \quad .$$

ACKNOWLEDGMENTS

Many members of the Berkeley scientific community have contributed to this research. In particular, I wish to thank glass-blower Dane Anderberg for excellent workmanship on the thallium cell. I also thank Persis S. Drell for a great deal of experimental assistance in the early stages of this work and in particular for introducing me to lasers. In addition, I am grateful to James D. Garnett for aid and helpful discussions.

Most of all, I acknowledge my adviser, Eugene D. Commins, for his contributions to every aspect of this work. His encouragement and confidence in me have been a continuous source of inspiration. In particular, I thank him for the education I have received under his guidance.

This research was supported by the Director, Office of Energy Research, Office of Basic Energy Sciences, Chemical Sciences Division of the U.S. Department of Energy under Contract No. DE-AC03-76SF00098. Laser equipment used in this work is borrowed from the San Francisco Laser Center, supported by the National Science Foundation, NSF Grant No. CHE79-16250 and the National Institute of Health, NIH Grant No. P41 RR01613-02 awarded to the University of California at Berkeley in collaboration with Stanford University.

This thesis is dedicated to my family for their support and encouragement throughout the years.

REFERENCES

1. Arnison, G., et al. Phys. Lett. 122B, 103 (1983).
2. Arnison, G., et al. Phys. Lett. 126B, 398 (1983).
3. Bucksbaum, P.H., E.D. Commins, and L.R. Hunter. Phys. Rev. D 24, 1134 (1981).
4. Commins, E.D., and P.H. Bucksbaum. Weak Interactions of Leptons and Quarks. Cambridge Univ. Press, Cambridge (1983).
5. Chu, S., E.D. Commins, and R. Conti. Phys. Lett. A 60, 96 (1977).
6. Das, B.P., private communication (1985).
7. Drell, P., and S. Chu. Opt. Comm. 28, 343 (1979).
8. Drell, P.S. Ph.D. thesis, University of California (1983).
9. Drell, P.S. and E.D. Commins. Phys. Rev. Lett. 53, 968 (1984).
10. Drell, P.S. and E.D. Commins. Phys. Rev. A 32, 2196 (1985).
11. Gallagher, A. and A. Lurio. Phys. Rev. 136A, 87 (1964).
12. Glashow, S.L. Nucl. Phys. 22, 579 (1961).
13. Hsieh, J.C. and J.C. Baird. Phys. Rev. A 6, 141 (1972).
14. Johnson, W.R., D.S. Guo, M. Idrees, and J. Sapirstein. Phys. Rev. A 32, 2093 (1985).
15. Johnson, W.R. and J. Sapirstein, private communication (1985).
16. Kasha, M. Journal Opt. Soc. Am. 38, 929 (1948).
17. Landau, L.D. and E.M. Lifshitz. Statistical Physics, vol. 1, 3rd edit. Pergamon Press, Oxford (1980).
18. Martensson-Pendrill, A.M., private communication (1985).
19. Nesmayonov, A.N. Vapor Pressure of the Chemical Elements. Elsevier Publishing Company, Amsterdam (1963).

20. Neuffer, D. and E.D. Commins. Phys. Rev. A 16, 844 (1977).

21. Prescott, C.Y., et al. Phys. Lett. B 77, 347 (1978).

22. Prescott, C.Y., et al. Phys. Lett. B84, 524 (1979).

23. Salam, A. Nobel Symposium No. 8, p. 367, ed. N. Svartholm. Almquist and Wiksell, Stockholm (1968).

24. Weast, R.C., ed. CRC Handbook of Chemistry and Physics, 62nd edit. CRC Press, Inc., Boca Raton, Florida (1981-82).

25. Weinberg, S. Phys. Rev. Lett. 19, 1264 (1967).